# 國　立　交　通　大　學

## 電信工程學系碩士班

## 碩士論文

# IEEE 802.11n 外部接收機設計

# Outer Receiver Designs for IEEE 802.11n System

研 究 生：沈士琦

指導教授：吳 文 榕　博士

中華民國九十五年七月

# IEEE 802.11n 外部接收機設計

# Outer Receiver Designs for IEEE 802.11n System

研 究 生：沈士琦　　Student：Shih-Chi Shen

指導教授：吳文榕 博士　　Advisor：Dr. Wen-Rong Wu

國 立 交 通 大 學

電信工程學系碩士班

碩 士 論 文

A Thesis

Submitted to Department of Communication Engineering

College of Electrical Engineering

National Chiao-Tung University

in Partial Fulfillment of the Requirements

for the Degree of

Master of Science

In

Communication Engineering

July 2006

Hsinchu, Taiwan, Republic of China

中華民國九十五年七月

# IEEE 802.11n 外部接收機設計

研究生：沈士琦　　指導教授：吳文榕 教授

國立交通大學電信工程學系碩士班

## 摘要

IEEE 802.11n 使用多輸入多輸出(MIMO)-正交分頻多工(OFDM)系統與位元交錯調變碼(BICM)做為其基頻傳輸技術。在此論文，我們著重在 802.11n 外部接收機設計。外部接收機主要包括軟性位元產生器與 Viterbi 解碼器。我們採用兩種方式來獲得軟性位元資訊。第一種方式為最小均方差(MMSE)等化器與多個軟性位元反對映器，第二種方式為名單球解碼(LSD)偵測器與向量軟性位元反對映器。雖然第二種方式有較佳的效能表現，但其運算複雜度較高。為了解決此問題，我們提出一個新的解碼調變方法，稱為頻帶交錯調變碼(TICM)。與 BICM 不同的地方在於 TICM 將軟性位元反對映器併入 Viterbi 解碼器。LSD 偵測器也能用來化簡 TICM 的運算複雜度。在 802.11n 系統下，模擬證明 TICM 的解碼運算複雜度低於 BICM，且效能優於 BICM。

Outer Receiver Designs for IEEE 802.11n System

Student: Shih-Chi Shen Advisor: Dr. Wen-Rong Wu

Department of Communication Engineering
National Chiao-Tung University

# Abstract

IEEE 802.11n uses the MIMO-OFDM along with bit-interleaved coding modulation (BICM) as its baseband transmission scheme. In this thesis, we will focus on the outer receiver design for the IEEE 802.11n system. The outer receiver mainly consists of a soft-bit computing device and a Viterbi decoder. Two approaches are studied to obtain soft-bit information. The first one uses a minimum mean-square error (MMSE) equalizer followed by multiple scalar soft-bit demappers. The second one involves a list sphere decoding (LSD) detector and a vector demapper. Though the later approach can have excellent performance, its computational complexity is high. To solve the problem, we then propose a new coding-modulation scheme, referred to as tone-interleaved coded modulation (TICM). Different from BICM, TICM merges the soft-bit demapping process into the Viterbi structure. The LSD algorithm can also be applied in TICM resulting in a low-computational algorithm. Simulations with the 802.11n system show that while the computational complexity of the demodulation of TICM is lower than that of BICM, its performance can be much better.

# 誌謝

本篇論文得以順利完成，首先要特別感謝我的指導教授　吳文榕博士，在課業學習與論文研究上不厭其煩的引導我正確的方向。

另外，我要感謝曾鼎哲學長、黃朝旺學長、許兆元學長、李彥文學長、李俊芳學長與楊華龍學長等在研究上不吝指導，且同時感謝寬頻傳輸與訊號處理實驗室所有同學與學弟妹們的幫忙，尤其特別感謝龍星宇同學和我頻繁的討論，並給我許多建議。最後感謝我家人，給予我在精神上最大的鼓勵與支持，使得我可以順利地完成碩士學位。

# Contents

# List of Tables



# List of Figures

# Chapter 1 Introduction

Due to a fast growth, exiting wireless communication systems are not able to meet the demands. Increasing the transmission bandwidth is one way to alleviate the problem. However, the available spectrum is limited. Another approach is to increase the efficiency of spectrum usage. Advances in coding, such as turbo codes [1] and low-density parity-check (LDPC) codes [2], have made the transmission rate approach the shannon bound [3]. Conventionally, the communication system is implemented as a single-input single-output (SISO) system. It has been shown that in a rich scattering environment, an effectively way to improve spectrum efficiency is to use a multi-input multi-output (MIMO) system. Telartar and Foschini have shown that the MIMO channel capacity [4], [5] will grow approximately linearly with the number of antennas used. This capacity indicates the potential spectrum efficiency we can enhance.

Orthogonal frequency division multiplexing (OFDM), proposed by Salzberg in 1967 [6], is known to have high spectrum efficiency and good resistance against multi-path interference. Moreover, duplexing and multiple accesses can be easily implemented with a frequency division manner. Due to the hardware implementation problem, this modulation technique was not widely used until discrete Fourier transform (DFT) was developed by Weistein and Ebert in 1971 [7]. Nowadays, OFDM becomes one of the most popular techniques in wired and wireless communications. Combining with the MIMO structure, OFDM can further enhance the spectrum efficiency.

The main obstacle for wireless mobile communication is the fading channel effect. A simple and effective method for this problem is bit-interleaved coded modulation (BICM), proposed by Zehavi in 1992 [8]. Then main idea is to use a

bit-level interleaver between an encoder and a modulator so that in a deep fade period, bursty errors can be avoided and the overall coding gain can be improved. The BICM scheme has been widely used in OFDM systems.

To develop the next generation of wireless local area networks (WLAN), IEEE announced an 802.11n Task Group (TGn) in January 2004. The target data rate for the new standard have a theoretical bount of 540Mbit/s. In other word, it should be 100 times faster than 802.11b, or 10 times faster than 802.11a/11g. It is expected that 802.11n will also offer a better operating distance than current 802.11 networks. The modulation of 802.11n uses the MIMO-OFDM and BICM techniques such that the throughput can be significantly increased and the channel fading effect can be minimized. Since that TGn Sync is one of the major competing groups of 802.11n, we use its proposal released by TGn Sync in July 2005 [14] as our simulation platform in the rest of this thesis.

However, when the MIMO-OFDM system with BICM is used, all spatial streams from different transmit antennas will interfere with each another at the receive antennas. A simple solution for this problem is to use an equalizer to suppress the interference, and then transform the MIMO system into multiple SISO systems. Then, the standard method for BICM demodulation can be applied. Commonly used equalizers include the zero-forcing (ZF) equalizer and the minimum mean-square error (MMSE) equalizer. If the convolutional coding is used, the Viterbi algorithm [12] will be a natural choice for the decoder. In this case, we then need to have a soft-bit demapper to calculate the bit metrics for the equalized symbol [9]. The demapper developed for the SISO-OFDM system can be straightforwardly extended to the MIMO-OFDM system.

The approach outline above is conceptually simple and easy to be implemented. However, it is not optimal. This is due to the fact that after the equalization, noise

components at the receive antennas become correlated. The MIMO system cannot be transferred into multiple independent SISO systems. Recently, a soft detector, named list sphere decoding (LSD) was proposed [11]. The LSD is a “list” version of the sphere decoding [10], which is an efficient method for maximum likelihood (ML) estimator for the MIMO system. With a simple modification of the original sphere decoding, LSD provides a list of candidates that allows us to compute the optimum soft-bit metrics.

Even with LSD, the demodulation process for the MIMO-OFDM system with BICM is still complicated and the required memory size is large, particular for high-through rate scenarios. To overcome the problem, we propose a new scheme, called tone-interleaved coded modulation (TICM), in the second part of this thesis. The main difference between BICM and TICM is the level of interleaver used in the system. The interleaver at the BICM transmitter uses a bit as its basic unit while that at the TICM transmitter uses a block of symbols as its basic unit. The symbols in a block are those transmitted at a single tone at a time instant. This results in different receiver architectures for BICM and TICM. To further simplify the computational complexity of TICM, we proposed a suboptimal method involving path-reduction in the Viterbi algorithm, and the extended use of the LSD detector at the branch metric (BM) calculation. Simulations show that the proposed TICM scheme can have better performance while the computational complexity is lower.

The rest of this thesis is organized as follows. In Chapter 2, we describe the TGn Sync proposal for 802.11n [14], the MIMO channel models provided by TGn Sync [15], and the fundamental MIMO-OFDM system. In Chapter 3, we present the conventional demodulation for the MIMO-OFDM system with BICM, involving the MMSE equalizer, the soft-bit demmapper, and the Viterbi decoder. Also, we will describe the LSD detector. In Chapter 4, we present the proposed TICM scheme and

its suboptimal demodulation method. The performance and computational complexity of BICM and TICM are also compared. Finally, we give some conclusions and outline future works in Chapter 5.

# Chapter 2 System Model

## 2.1 Introduction to the TGn Sync Proposal

The block diagram of the transmitter in the TGn Sync proposal is shown in Fig. 2-1.

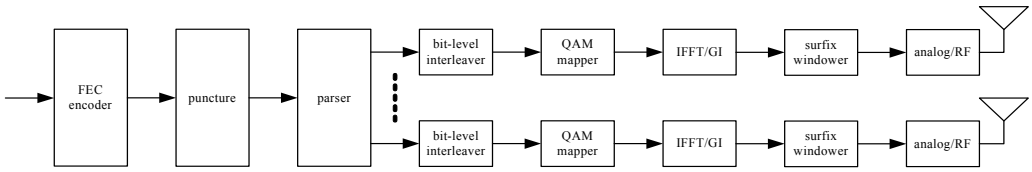


Fig. 2-1: The block diagram of the transmitter in the TGn Sync proposal

The mandatory number of spatial streams is two and the mandatory channelization bandwidth is 20MHz. The proposal also utilizes optional techniques such as four spatial streams, and 40MHz channelization bandwidth. Table 2-1 shows the primary parameters in the TGn Sync proposal.

| Parameter | Mandatory | Optional |
|---|---|---|
| Number of Spatial Streams | 1 and 2 | 3 and 4 |
| Number of Transmit Antennas | 2 | Greater than 2 |
| Channelization bandwidth | 20MHz | 40MHz |
| Number of Occupied Sub-channels | 56 in 20MHz | 114 in 40MHz |
| Number of Data Sub-channels | 52 | 108 |
| Number of Pilot Sub-channels | 4 | 6 |
| Modulation Type | BPSK, QPSK, 16-QAM, 64-QAM | 256-QAM |
| Code Rate | 1/2, 2/3, 3/4, 5/6 | |
| Guard Interval | 800ns | 400ns |
| Convolutional Coding | $R_c = 1/2, K_{CC} = 7$ | |
| LDPC | | TX and RX Optional |

Table 2-1: The primary parameters in the TGn Sync proposal

### 2.1.1 Preamble Format

The generic format of PPDU is shown in Fig. 2-2.


Fig. 2-2: PPDU format

Legacy Short Training Field (L-STF), Legacy Long Training Field (L-LTF), Legacy Signal Field (L-SIG), and High Throughput Signal Field (HT-SIG) comprise the legacy compatible part of the PPDU preamble. High Throughput Short Training Field (HT-STF), High Throughput Long Training Field (HT-LTF), and High Throughput Data (HT-Data) comprise the HT-Part of the PPDU. The functions operated with the preamble include packet detection, auto gain control (AGC), coarse frequency offset estimation, coarse timing offset estimation, fine frequency offset estimation, fine timing offset estimation, and channel estimation.

### 2.1.2 FEC Encoder

The mandatory coder is the convolutional code (CC) encoder and the optional one is a low-density parity-check (LDPC) encoder. In our simulation platform, the transmitter is implemented by the mandatory encoder shown in Fig. 2-3 with $K_{CC} = 7$ and $R_c = 1/2$, where $K_{CC}$ represents the constraint length of the CC encoder, and $R_c$ represents the code rate of the CC encoder.

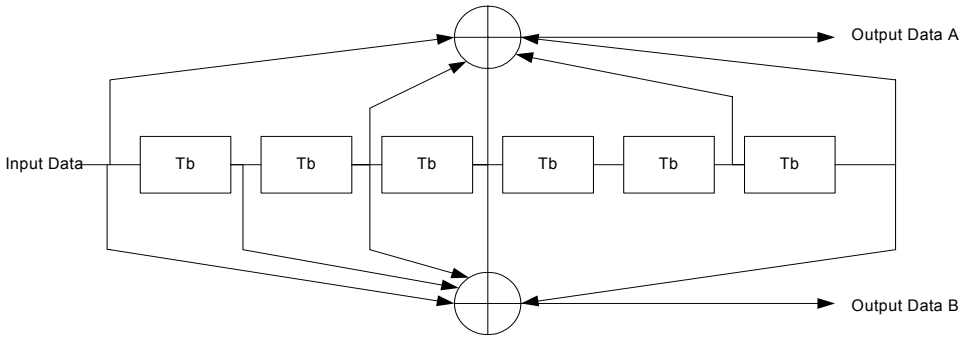


Fig. 2-3: The CC encoder with $K_{CC} = 7$

### 2.1.3 Puncturer

In order to support variable code rates, encoded bits may be punctured. In TGn Sync, three kinds of code rate are defined, which are 2/3, 3/4 and 5/6. The procedure of puncturing is shown in Fig. 2-4.

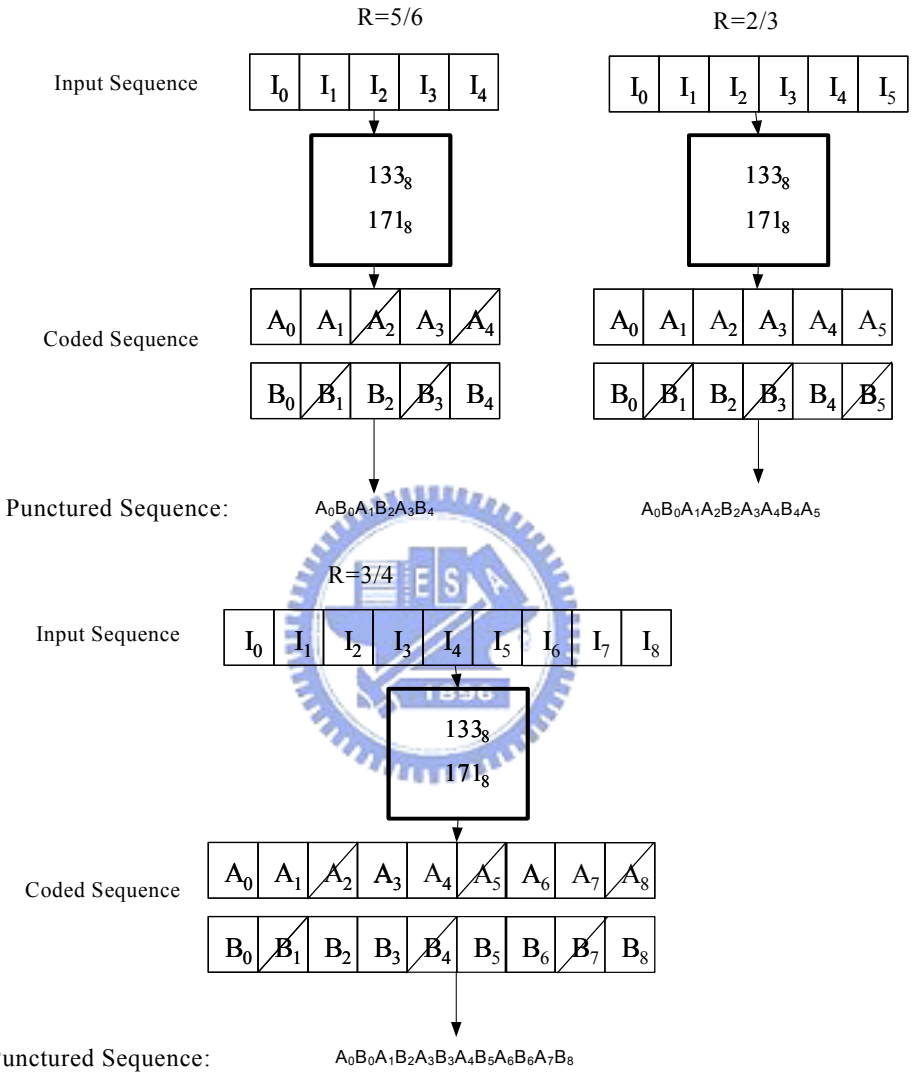


Fig. 2-4: The procedure of puncturing in the TGn Sync proposal

### 2.1.4 Parser

Encoded and punctured bits are parsed to multiple spatial streams by a round-robin parser. Define

$$s = \max\left\{\frac{N_{bpsc}}{2}, 1\right\} \tag{2.1}$$

where $N_{bpsc}$ represents the number of bits transmitted per sub-channel. The parser repeatedly sends consecutive $s$ bits to different antennas.

### 2.1.5 Interleaver

To have the frequency diversity gain and reduce the spatial correlation of the MIMO channel, the proposal utilizes a space-frequency bit-level interleaver shown in Fig. 2-5.

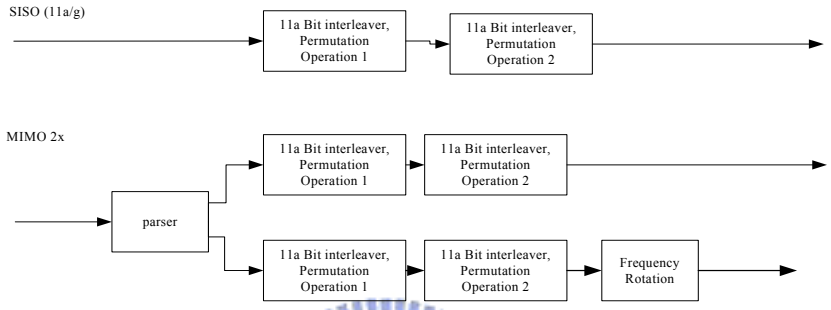


Fig. 2-5: The space-frequency bit-level interleaver in the TGn Sync proposal

Coded and punctured bits are interleaved across spatial streams and frequency tones by a three-step permutation. Table 2-2 defines the parameters used in the interleaver.

| | $N_{column}$ | $N_{row}$ | $N_{rot}$ |
|---|---|---|---|
| 20 MHz channels | 13 | $4N_{BPSC}$ | 11 |
| 40 MHz channels | 18 | $6\ N_{BPSC}$ | 29 |

Table 2-2: The parameters used in the interleaver

The first permutation is defined by the rule as

$$i = N_{row} \times \left(k \bmod N_{column}\right) + \text{floor}\left(k / N_{column}\right), k = 0,1,\ldots, N_{CBPS} - 1 \qquad (2.2)$$

The second permutation is defined by the rule as

$$j = s \times \text{floor}\left(i / s\right) + \left(i + N_{CBPS} - \text{floor}\left(N_{column} \times i / N_{CBPS}\right)\right) \bmod s, i = 0,1,\ldots, N_{CBPS} - 1 \qquad (2.3)$$

The third permutation is defined by the rule as

$$r = \left( j - \left( \left( 2 \times i_{ss} \right) \bmod 3 + 3 \times \text{floor}(i_{ss} / 3) \right) \times N_{rot} \times N_{BPSC} \right) \bmod N_{CBPS}, j = 0,1,\ldots,N_{CBPS} - 1 \quad (2.4)$$

where $i_{SS} = 0,1,\ldots,N_{SS} - 1$ is the index of the spatial stream on which this interleaver is operating.

### 2.1.6 QAM Mapper

The QAM mapping scheme is the same with that in 802.11a. The QAM constellation is the gray-mapping square QAM constellation. The constellation of BPSK, QPSK and 16-QAM are shown in Fig. 2-6, and the constellation of 64-QAM is shown in Fig. 2-7.

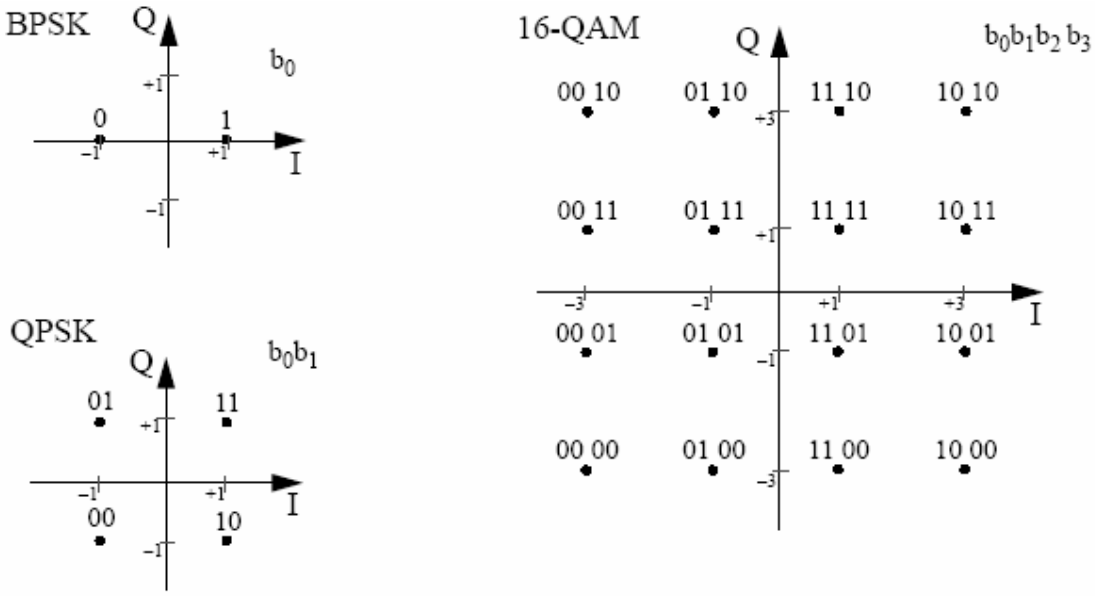


Fig. 2-6: BPSK, QPSK and 16-QAM constellation

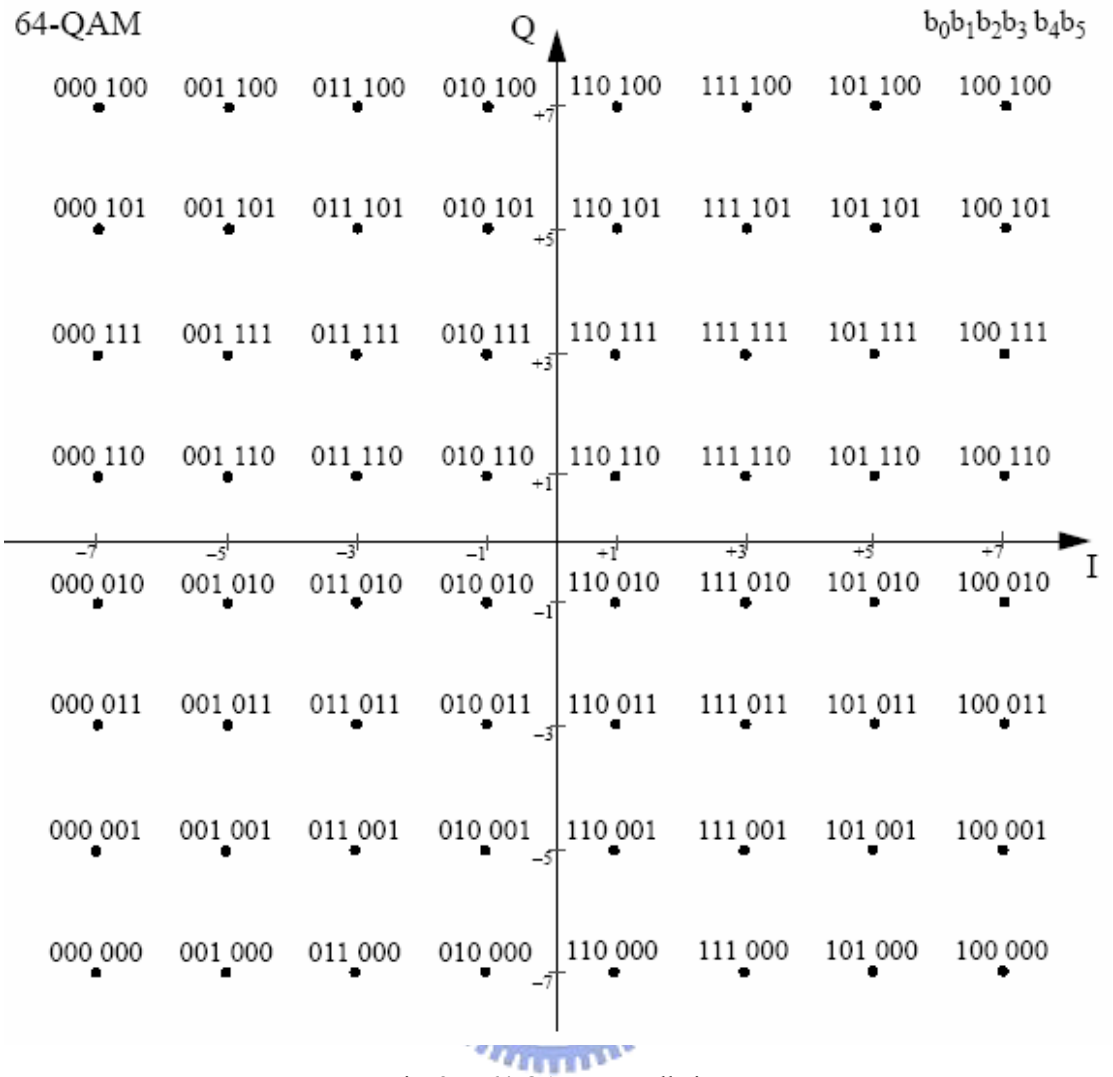


Fig. 2-7: 64-QAM constellation

### 2.1.7 Surfix Windower

To suppress the side-lobs of the transmitted signal, a surfix windower is added after IFFT/GI. For 20MHz channelization, we can copy the seventeenth sample to the end of an OFDM symbol (as shown in Fig. 2-8), divide the first and last sample of the OFDM symbol by 2, and overlap-and-add it with other symbols (as shown in Fig. 2-8).

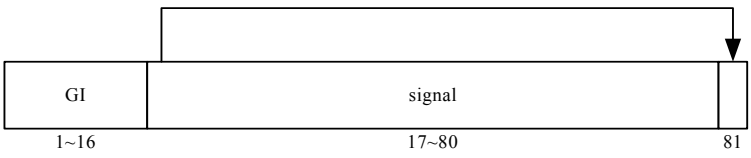


Fig. 2-8: The surfix windower at 20MHz channelization

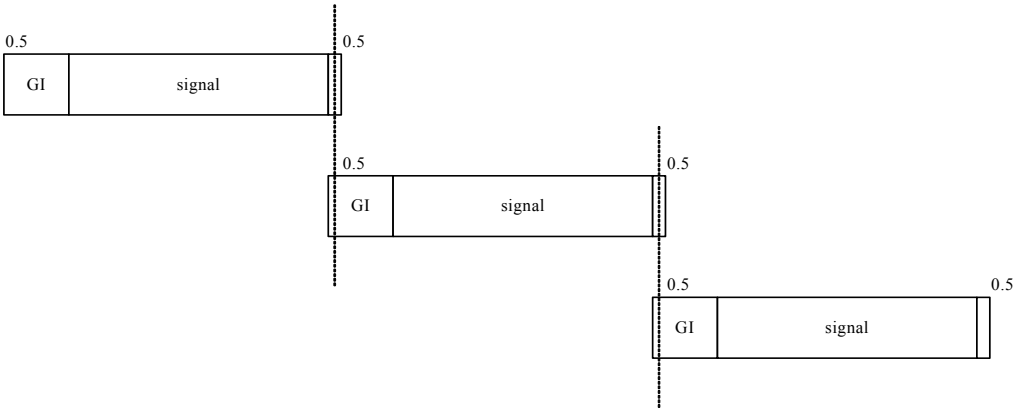


Fig. 2-9: The procedure of concatenating the modified transmitted signal

## 2.2 MIMO Channel Model

There are six channel models, A, B, C, D, E and F, provided by TGn Sync [15] for 802.11n. The environments for these channel models can be described as follows.

(Channel-A). a typical office environment, non-line-of-sight (NLOS) conditions, and 50 ns rms delay spread

(Channel-B). a typical large open space and office environments, NLOS conditions, and 100 ns rms delay spread

(Channel-C). a large open space (indoor and outdoor), NLOS conditions, and 150 ns rms delay spread

(Channel-D). the same as model C, line-of-sight (LOS) conditions, and 140 ns rms delay spread (10 dB Ricean *K*-factor at the first delay)

(Channel-E). a typical large open space (indoor and outdoor), NLOS conditions, and 250 ns rms delay spread

Properties of these models are shown in Table 2-3 and Table 2-4. Here, *K*-factor for LOS condition applies only to the first tap, and $K\text{-}factor = -\infty(dB)$ applies to all other taps. There is another factor $d_{BP}$ called the breakpoint distance. If the transmit-receive separation distance is set less than $d_{BP}$, the channel will be considered as the LOS condition. If the transmit-receive separation distance is greater

than $d_{BP}$, the channel will be considered as the NLOS condition.

| Model | Condition | K-factor (dB) | RMS delay spread (ns) | # of clusters |
|---|---|---|---|---|
| **A (optional)** | LOS/NLOS | 0/ -∞ | 0 | 1 tap |
| **B** | LOS/NLOS | 0 / -∞ | 15 | 2 |
| **C** | LOS/NLOS | 0 / -∞ | 30 | 2 |
| **D** | LOS/NLOS | 3 / -∞ | 50 | 3 |
| **E** | LOS/NLOS | 6 / -∞ | 100 | 4 |
| **F** | LOS/NLOS | 6 / -∞ | 150 | 6 |

Table 2-3: Model parameters for LOS/NLOS conditions

| New Model | $d_{BP}$ (m) | Slope before $d_{BP}$ | Slope after $d_{BP}$ | Shadow fading std. dev. (dB) before $d_{BP}$ (LOS) | Shadow fading std. dev. (dB) after $d_{BP}$ (NLOS) |
|---|---|---|---|---|---|
| A (optional) | 5 | 2 | 3.5 | 3 | 4 |
| B | 5 | 2 | 3.5 | 3 | 4 |
| C | 5 | 2 | 3.5 | 3 | 5 |
| D | 10 | 2 | 3.5 | 3 | 5 |
| E | 20 | 2 | 3.5 | 3 | 6 |
| F | 30 | 2 | 3.5 | 3 | 6 |

Table 2-4: Path loss model parameters

We choose the channel-B (NLOS) with distance 6m, channel-D (NLOS) with distance 11m, and channel-E (NLOS) with distance 21m as our simulation environments in this thesis. Besides, the time resolution of the channel model is 10ns, which is one-fifth of the sampling period (3.2ms/64=50ns). We oversample the transmitted signal by a factor of 5 and interpolate it linearly in order to convolve with the response generated by the channel model. The block diagram of the MIMO channel model is shown in Fig. 2-10.

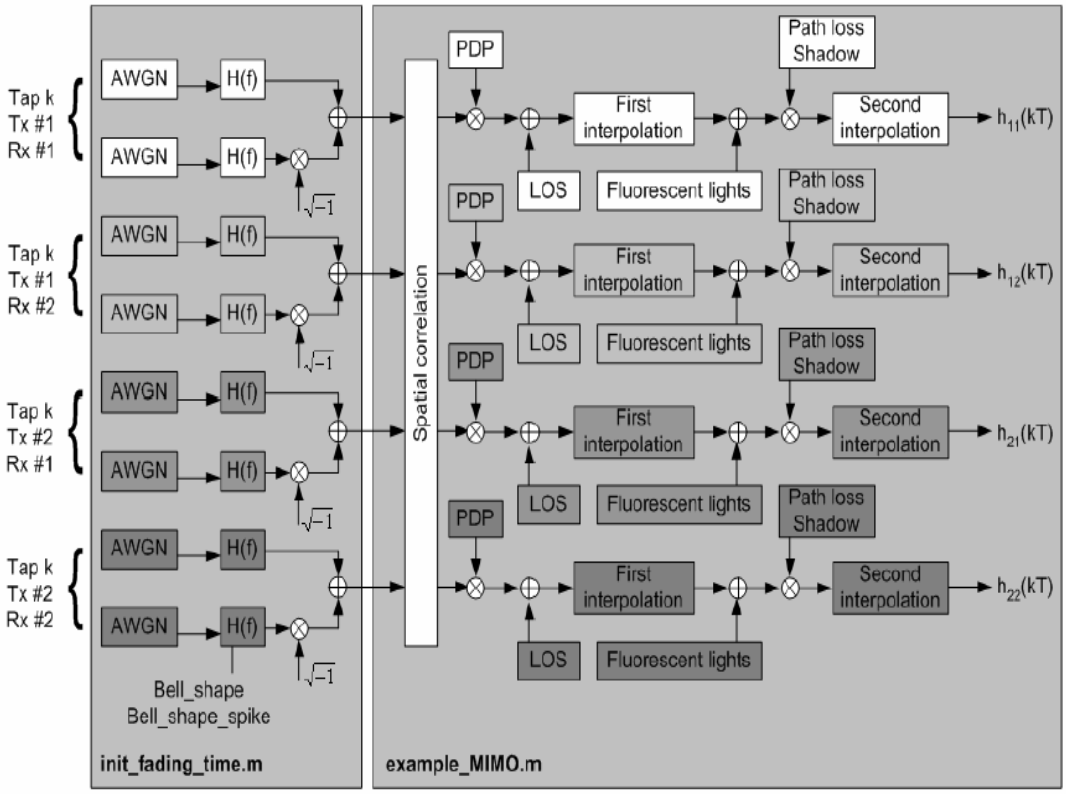


Fig. 2-10: The block diagram of the MIMO channel model

## 2.3 MIMO-OFDM System Model

Before our formal development, we define notations will be used in the sequel. Scalars are denoted in lower case letters, vectors in lower case bold letters, and metrics in upper case bold letters. Also, $[.]^T$ and $[.]^H$ indicate the transpose and conjugate transpose of a vector or matrix inside the bracket respectively. Since 802.11n is designed to be used in the indoor environment, we can assume that the MIMO channel is a multi-path quasi-static Rayleigh fading channel. The frequency response of the MIMO channel at the $k^{th}$ sub-channel is defined as

$$\mathbf{H}^k = \begin{bmatrix} h_{1,1}^k & \cdots & h_{1,N_T}^k \\ \vdots & h_{q,p}^k & \vdots \\ h_{N_R,1}^k & \cdots & h_{N_R,N_T}^k \end{bmatrix} \tag{2.5}$$

where $p$ represents the index of the transmit antenna, $q$ the index of the receive

antenna, $N_T$ the number of transmit antennas, and $N_R$ the number of receive antennas. The transmitted signal vector at the $k^{th}$ sub-channel and the $l^{th}$ OFDM symbol before IFFT/GI is defined as

$$\mathbf{s}^{l,k} = \left[ s_1^{l,k}, \cdots, s_{N_T}^{l,k} \right]^T \tag{2.6}$$

The received signal vector at the $k^{th}$ sub-channel and the $l^{th}$ OFDM symbol after GI-Remover/FFT is defined as

$$\mathbf{r}^{l,k} = \left[ r_1^{l,k}, \cdots, r_{N_R}^{l,k} \right]^T \tag{2.7}$$

Assume that there are no inter symbol interference (ISI) and inter carrier interference (ICI). Then, $\mathbf{r}^{l,k}$ can be represented as

$$\mathbf{r}^{l,k} = \mathbf{H}^k \cdot \mathbf{s}^{l,k} + \mathbf{n}^{l,k} \tag{2.8}$$

where

$$\mathbf{n}^{l,k} = \left[ n_1^{l,k}, \cdots, n_{N_R}^{l,k} \right]^T \tag{2.9}$$

is the received noise vector, and each element in $\mathbf{n}_{l,k}$ is statistically independent and identically distributed (i.i.d.) complex Gaussian random variable with zero mean and variance $\sigma^2 = \sigma_I^2 + \sigma_Q^2 = N_0$. Signal to noise ration (SNR) is defined as the average received power per receive antenna divided by the average noise power.

$$SNR = \frac{E\left\{ \left| r_q'(t) \right|^2 \right\}}{\sigma^2} \tag{2.10}$$

where $r_q'(t)$ represents the received signal at time $t$ at the $q^{th}$ transmit antenna. For simplicity, we ignore the index $k$ and $l$ in the rest of this thesis. Then, we have

$$\mathbf{r} = \mathbf{H} \cdot \mathbf{s} + \mathbf{n} \tag{2.11}$$

# Chapter 3 MIMO-OFDM with BICM

## 3.1 Bit-Interleaved Coded Modulation

Originally proposed by Zehavi [8], BICM inserts a bit-level interleaver between the encoder and modulator. With this operation, bursty bit errors can be reduced, and the correction capability of the decoder can be enhanced. As a result, BICM is suited to the fast fading channel environment. For non-fading frequency-selective channels, BICM can be cooperated with OFDM to have frequency diversity gain. Besides, when the MIMO structure is added, spatial diversity can be achieved as well. We will review two existing demodulation schemes for BICM operated in a MIMO-OFDM system. The first one is suboptimal. It uses a MMSE equalizer to suppress the interference arising in the MIMO system, and then transfer the MIMO system into multiple SISO systems. Finally, it applies one-dimensional soft-bit demappers obtaining soft-bit information for the received signal. The second one is optimal. It uses the LSD to find candidates for original transmitted symbol vectors. Then, soft-bit information is calculated from these candidates. In this case, the soft-bit demapper is multi-dimensional.

## 3.2 Suboptimal Receiver with the MMSE Equalizer

This approach includes operations such as MMSE equalization, soft-bit demapping and soft-input Viterbi decoding. First, the received signal vector is processed by the MMSE equalizer. The resultant signal vector is assumed to be decoupled. As a result, we can transfer the MIMO system into multiple SISO systems. For each SISO system, a soft-bit demapper can be applied to obtain soft-bit information for the corresponding bit stream. Finally, the soft bits are fed into the soft-input Viterbi decoder. The block diagram of the MIMO-OFDM transceiver is

shown in Fig. 3-1 and Fig. 3-2.

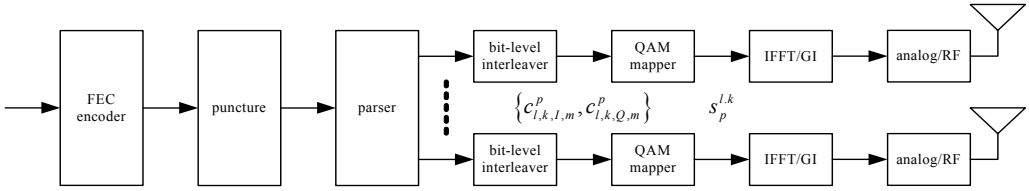


Fig. 3-1: The block diagram of the MIMO-OFDM transmitter for BICM

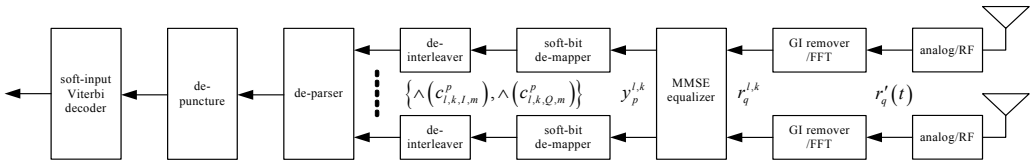


Fig. 3-2: The block diagram of the MIMO-OFDM receiver using the MMSE equalizer for BICM

### 3.2.1 Simplified Soft-Bit Demapper for SISO-OFDM System

We leave the development of the MMSE equalizer in a later subsection. Here, we start with the soft-bit demapper for the SISO system. Let $M$ be the number of symbols for the gray-mapping square QAM, where $N_{bpsc} = \log_2 M$ represents the number of bits transmitted per sub-channel at a time instant. So that $N_{bpsc}/2$ interleavered bits are mapped into the in-phase and quadrature-phase components of the complex QAM symbol. The received signal is expressed in (2.11). Here, we omit the index $p$ and the index $q$ for simplicity since $N_T = 1$ and $N_R = 1$. Then, (2.11) can be simplifed as

$$r = h \cdot s + n \tag{3.1}$$

Each $s$ is mapped from the QAM mapper according to the corresponding bit sequence, $\left\{c_{I,1}, \cdots, c_{I,m}, \cdots, c_{I,N_{bpsc}/2}, c_{Q,1}, \cdots, c_{Q,m}, \cdots, c_{Q,N_{bpsc}/2}\right\}$, where $m$ represents the bit index of the QAM constellation. We define the four metrics for each $r$ as

$$\begin{aligned} m_z\left(c_{I,m}\right) &= \max_{\varphi \in \psi^{(z)}_{I,m}} \ln p\left[r \middle| s = \varphi\right], z = 0,1 \\ m_z\left(c_{Q,m}\right) &= \max_{\varphi \in \psi^{(z)}_{Q,m}} \ln p\left[r \middle| s = \varphi\right], z = 0,1 \end{aligned} \tag{3.2}$$

where $\varphi$ represents the hypothesized transmitted signal, $\psi_{I,m}^{(z)}$ the subset of all symbols with $c_{I,m}=z, z=0,1$, and $\psi_{Q,m}^{(z)}$ the subset of all symbols with $c_{Q,m}=z, z=0,1$. Assume that the channel is memoryless and define the bit metric of $c_{I,m}$ for BICM as

$$\wedge\left(c_{I,m}\right) \triangleq \ln\left(\frac{p\left[c_{I,m}=1\middle|r\right]}{p\left[c_{I,m}=0\middle|r\right]}\right) \tag{3.3}$$

A posteriori probability log likelihood ratio (LLR) can be shown to be

$$\ln\left(\frac{p\left[c_{I,m}=1\middle|r\right]}{p\left[c_{I,m}=0\middle|r\right]}\right)=\ln\left(\frac{\sum_{\varphi=\psi_{I,m}^{(1)}} p\left[s=\varphi\middle|r\right]}{\sum_{\varphi=\psi_{I,m}^{(0)}} p\left[s=\varphi\middle|r\right]}\right) \tag{3.4}$$

Applying the Bayes rule and assuming that all symbols on the constellation are transmitted with equal probability, we can rewrite (3.4) as

$$\ln\left(\frac{\sum_{\varphi=\psi_{I,m}^{(1)}} p\left[s=\varphi\middle|r\right]}{\sum_{\varphi=\psi_{I,m}^{(0)}} p\left[s=\varphi\middle|r\right]}\right)=\ln\left(\frac{\sum_{\varphi=\psi_{I,m}^{(1)}} p\left[r\middle|s=\varphi\right]}{\sum_{\varphi=\psi_{I,m}^{(0)}} p\left[r\middle|s=\varphi\right]}\right) \tag{3.5}$$

The suboptimal LLR can be obtained by the log-sum approximation: $\ln\left(\sum_i x_i\right)\approx \max_i \ln\left(x_i\right)$, which is a good approximation if the sum in the left-hand side of the equation is dominated by its largest term. This assumption can be hold when SNR is high. Then,

$$\wedge\left(c_{I,m}\right)\approx \ln\left(\frac{\max_{\varphi=\psi_{I,m}^{(1)}} p\left[r\middle|s=\varphi\right]}{\max_{\varphi=\psi_{I,m}^{(0)}} p\left[r\middle|s=\varphi\right]}\right)=m_1\left(c_{I,m}\right)-m_0\left(c_{I,m}\right) \tag{3.6}$$

In [9], a scheme that simplifies the calculation of the bit metrics was proposed. We now outline the scheme. Since the conditional PDF of $r$ obeys complex Gaussian distribution.

$$p\left[r\middle|s=\varphi\right]=\frac{1}{\pi\cdot\sigma^2}\exp\left\{-\frac{\left|r-h\cdot\varphi\right|^2}{\sigma^2}\right\} \tag{3.7}$$

Let $y=r/h$. Then $y$ can be expressed as

$$y=r/h=s+n/h \tag{3.8}$$

(3.6) can be modified as

$$\begin{aligned}\wedge\left(c_{I,m}\right)&=\frac{1}{\sigma^2}\left\{\min_{\varphi\in\psi_{I,m}^{(0)}}\left|r-h\cdot\varphi\right|^2-\min_{\varphi\in\psi_{I,m}^{(1)}}\left|r-h\cdot\varphi\right|^2\right\}\\&=\frac{\left|h\right|^2}{\sigma^2}\left\{\min_{\varphi\in\psi_{I,m}^{(0)}}\left|y-\varphi\right|^2-\min_{\varphi\in\psi_{I,m}^{(1)}}\left|y-\varphi\right|^2\right\}\end{aligned} \tag{3.9}$$

As we can observe, the two object symbols $\varphi$ nearest to the received equalized signal $y$ within disjointed subsets $\psi_{I,m}^{(0)}$ and $\psi_{I,m}^{(1)}$ always lie in the same row if the partition boundaries are vertical, or in the same column if the partition boundaries are horizontal. Then,

$$\begin{aligned}\wedge\left(c_{I,m}\right)&=\frac{\left|h\right|^2}{\sigma^2}\left\{\min_{\varphi\in\psi_{I,m}^{(0)}}\left|y^I-\varphi_I\right|^2-\min_{\varphi\in\psi_{I,m}^{(1)}}\left|y^I-\varphi_I\right|^2\right\}\\&=\frac{4\cdot\left|h\right|^2}{\sigma^2}\cdot\frac{1}{4}\left\{\min_{\varphi\in\psi_{I,m}^{\prime(0)}}\left|y^I-\varphi_I\right|^2-\min_{\varphi\in\psi_{I,m}^{\prime(1)}}\left|y^I-\varphi_I\right|^2\right\}\\&=CSI\cdot D_{I,m}\end{aligned} \tag{3.10}$$

where $y^I$ represents the real part of $y$ and $\psi_{I,m}^{\prime(z)}$ the subset containing the real parts of the complex symbols of $\psi_{I,m}^{(z)}, z=0,1$. The term $4\cdot\left|h\right|^2/\sigma^2$ can be seen as channel state information (CSI), which is proportional to the SNR at different sub-channel $k$. Take 16-QAM constellation, shown in Fig. 3-3, as an example. We can calculate $D_{I,m}$ as

$$D_{I,1} = \begin{cases} y^I & , |y_I| \le 2 \\ 2(y^I - 1) & , y_I > 2 \\ 2(y^I + 1) & , y_I < -2 \end{cases}$$
$$D_{I,2} = -|y^I| + 2 \tag{3.11}$$

With further simplification, (3.11) can be rewritten as

$$D_{I,m} \approx \begin{cases} y^I & , m = 1 \\ -|D_{I,m-1}| + d_{I,m} & , m > 1 \end{cases} \tag{3.12}$$

where $d_{I,m}$ represents one half of the distance between the partition boundaries of $c_{I,m}$. Similarly, $\wedge(c_{Q,m})$ can be derived as

$$\wedge(c_{Q,m}) = CSI \cdot D_{Q,m} \tag{3.13}$$

where

$$D_{Q,m} \approx \begin{cases} y^Q & , m = 1 \\ -|D_{Q,m-1}| + d_{Q,m} & , m > 1 \end{cases} \tag{3.14}$$

where $y^Q$ represents the imaginary part of $y$, and $d_{Q,m}$ one half of the distance between the partition boundaries of $c_{Q,m}$.

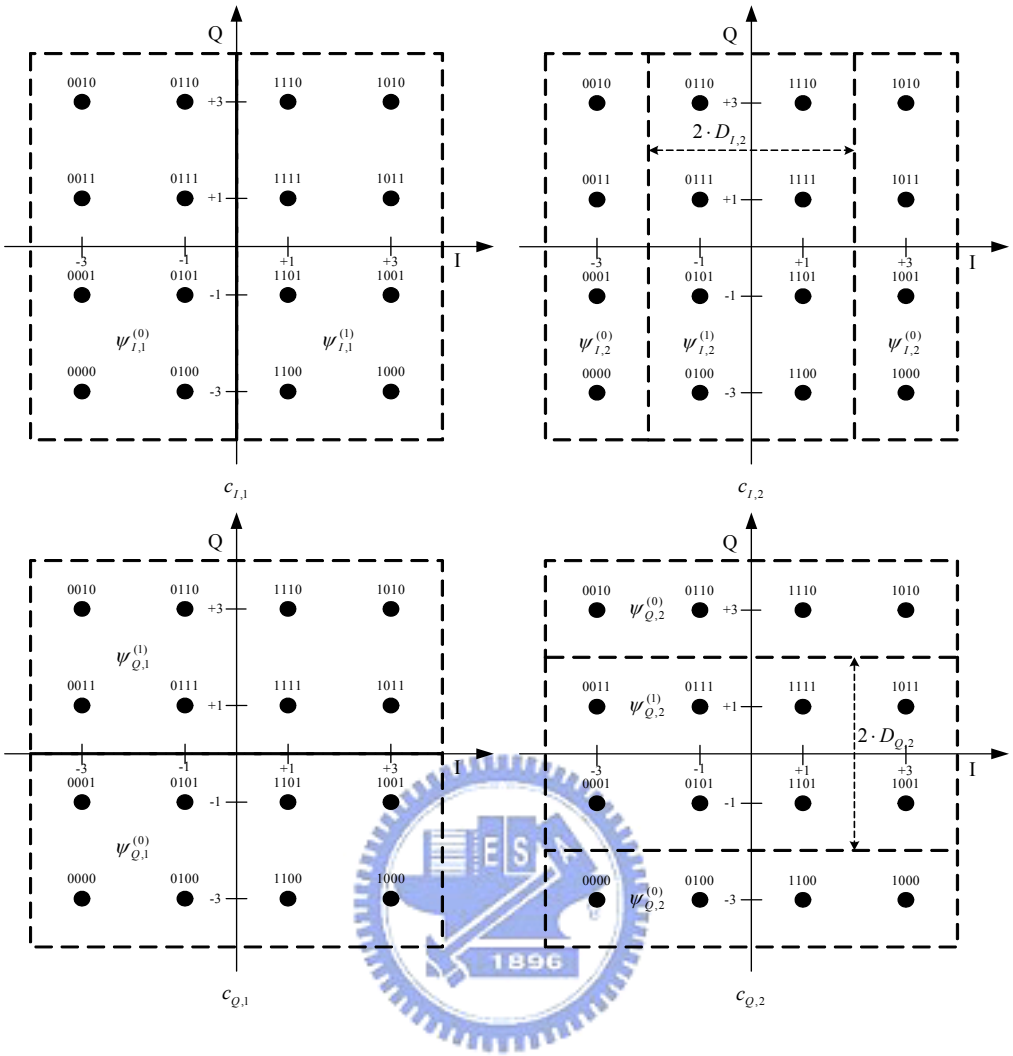


Fig. 3-3: 16-QAM constellation with $c_{I,1}$ and $c_{Q,1}$

The block diagram of the SISO-OFDM transceiver for BICM is shown in Fig. 3-4 and Fig. 3-5.

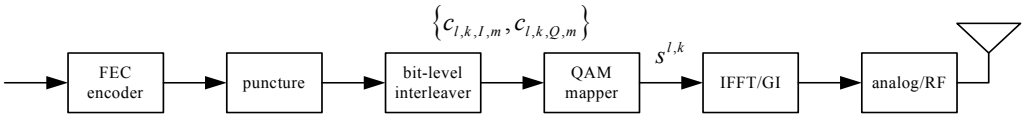


Fig. 3-4: The block diagram of the SISO-OFDM transmitter for BICM

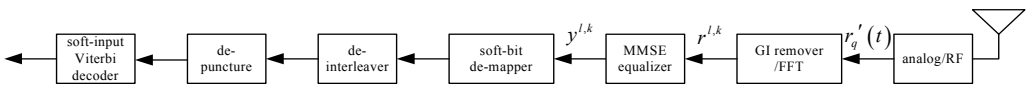


Fig. 3-5: The block diagram of the SISO-OFDM receiver using the MMSE equalizer for BICM

### 3.2.2 Simplified Soft-Bit Demapper for MIMO-OFDM System

Define the bit metric of $c_{I,m}^{p}$ as

$$\wedge\left(c_{I,m}^{p}\right) \triangleq \ln\left(\frac{p\left[c_{I,m}^{p}=1\middle|\mathbf{r}\right]}{p\left[c_{I,m}^{p}=0\middle|\mathbf{r}\right]}\right) \tag{3.15}$$

A posteriori probability log likelihood ratio can be shown to be

$$\ln\left(\frac{p\left[c_{I,m}^{p}=1\middle|\mathbf{r}\right]}{p\left[c_{I,m}^{p}=0\middle|\mathbf{r}\right]}\right)=\ln\left(\frac{\sum_{\boldsymbol{\varphi}=\boldsymbol{\psi}_{I,m}^{(1),p}} p\left[\mathbf{s}=\boldsymbol{\varphi}\middle|\mathbf{r}\right]}{\sum_{\boldsymbol{\varphi}=\boldsymbol{\psi}_{I,m}^{(0),p}} p\left[\mathbf{s}=\boldsymbol{\varphi}\middle|\mathbf{r}\right]}\right) \tag{3.16}$$

where $\boldsymbol{\varphi}=\left[\varphi_1\cdots\varphi_{N_T}\right]^T$ represents the hypothesized transmitted signal vector and $\boldsymbol{\psi}_{I,m}^{(z),p}$ the subset of all symbol vectors with $c_{I,m}^{p}=z, z=0,1$. Applying the Bayes rule and assuming that all symbols on the constellation are transmitted with equal probability, we can rewrite (3.16) as

$$\ln\left(\frac{\sum_{\boldsymbol{\varphi}=\boldsymbol{\psi}_{I,m}^{(1),p}} p\left[\mathbf{s}=\boldsymbol{\varphi}\middle|\mathbf{r}\right]}{\sum_{\boldsymbol{\varphi}=\boldsymbol{\psi}_{I,m}^{(0),p}} p\left[\mathbf{s}=\boldsymbol{\varphi}\middle|\mathbf{r}\right]}\right)=\ln\left(\frac{\sum_{\boldsymbol{\varphi}=\boldsymbol{\psi}_{I,m}^{(1),p}} p\left[\mathbf{r}\middle|\mathbf{s}=\boldsymbol{\varphi}\right]}{\sum_{\boldsymbol{\varphi}=\boldsymbol{\psi}_{I,m}^{(0),p}} p\left[\mathbf{r}\middle|\mathbf{s}=\boldsymbol{\varphi}\right]}\right) \tag{3.17}$$

Since that there are $2^{N_T\cdot N_{bpsc}}$ combinations of the transmitted signal vector $\mathbf{s}$ corresponding to the bit sequence $\left\{c_{I,1}^{1},\cdots,c_{I,N_{bpsc}/2}^{1},c_{Q,1}^{1},\cdots,c_{Q,N_{bpsc}/2}^{1},\cdots,c_{I,1}^{N_T},\cdots,c_{I,N_{bpsc}/2}^{N_T},c_{Q,1}^{N_T},\cdots,c_{Q,N_{bpsc}/2}^{N_T}\right\}$, evaluation of $\wedge\left(c_{I,m}^{p}\right)$ in (3.17) becomes quite complicated.

### 3.2.3 Minimum Mean-Square Error Equalizer

With the help of the MMSE approach equalizer, the MIMO-OFDM system can be decoupled into $N_T$ parallel SISO-OFDM systems. So, the scheme outlined in 3.2.1 can be extended its use from the SISO-OFDM system to the MIMO-OFDM system. The equalized signal vector is given by

$$\mathbf{y} = \left[ y_1 \cdots y_{N_T} \right]^T = \mathbf{G}_{MMSE}^H \cdot \mathbf{r} \tag{3.18}$$

where $G_{MMSE}$ can be found with an MMSE criterion. The criterion is to minimize the mean-square error between the equalized signal vector $\mathbf{y}$ and the transmitted signal vector $\mathbf{s}$. That is

$$\mathbf{G}_{MMSE} = \arg\min_{\mathbf{G}_{MMSE}} E\left\{ \left| \mathbf{y} - \mathbf{s} \right|^2 \right\} = \arg\min_{\mathbf{G}_{MMSE}} E\left\{ \left| \mathbf{G}_{MMSE}^H \cdot \mathbf{r} - \mathbf{s} \right|^2 \right\} \tag{3.19}$$

where

$$\mathbf{G}_{MMSE} = \begin{bmatrix} g_{1,1} & \cdots & g_{1,N_T} \\ \vdots & g_{q,p} & \vdots \\ g_{N_R,1} & \cdots & g_{N_R,N_T} \end{bmatrix} \tag{3.20}$$

Applying the Wiener-Hopf equation, we have

$$\mathbf{G}_{MMSE} = \left[ \mathbf{H} \cdot \mathbf{H}^H + \alpha \cdot \mathbf{I}_{N_R x N_R} \right]^{-1} \cdot \mathbf{H} \tag{3.21}$$

where $\alpha = \sigma^2 / \sigma_s^2$, $\sigma^2$ the variance of the additive complex Gaussian noise, and $\sigma_s^2$ the average transmitted signal power per transmit antenna. It is simple to derive the equalized signal $y_p$ for the $p^{th}$ transmit antenna as.

$$y_p = \left( \mathbf{g}_p \right)^H \cdot \mathbf{h}_p \cdot s_p + \left( \mathbf{g}_p \right)^H \cdot \sum_{i \neq p} \mathbf{h}_i \cdot s_i + \left( \mathbf{g}_p \right)^H \cdot \mathbf{n} \tag{3.22}$$

where

$$\begin{aligned} \mathbf{g}_p &= \left[ g_{1,p}, \cdots, g_{N_R,p} \right]^T \\ \mathbf{h}_p &= \left[ h_{1,p}, \cdots, h_{N_R,p} \right]^T \end{aligned} \tag{3.23}$$

We define the effective channel for the $p^{th}$ transmit antenna as

$$h_p^{eff} = \left( \mathbf{g}_p \right)^H \cdot \mathbf{h}_p \tag{3.24}$$

and the residual interference as

$$\mu_p = \left( \mathbf{g}_p \right)^H \cdot \sum_{i \neq p} \mathbf{h}_i \cdot s_i + \left( \mathbf{g}_p \right)^H \cdot \mathbf{n} \tag{3.25}$$

Then, we have

$$y_p = h_p^{eff} \cdot s_p + \mu_p \tag{3.26}$$

We assume that $\mu_p$ is complex Gaussian distributed. Since $s_1, \cdots, s_{N_T}$ and $n_1, \cdots, n_{N_R}$ are i.i.d. random variables, we can have

$$\sigma_{\mu_p}^2 = \sigma_s^2 \cdot \sum_{i \neq p} \left| \left( \mathbf{g}_p \right)^H \cdot \mathbf{h}_i \right|^2 + \sigma^2 \cdot \sum_{q=1}^{N_R} \left| g_{p,g} \right|^2 \tag{3.27}$$

Then,

$$p\left[ y_p \left| s_p = \varphi \right. \right] = \frac{1}{\pi \cdot \sigma_{\mu_p}^2} \exp\left\{ - \frac{\left| y_p - h_p^{eff} \cdot \varphi \right|^2}{\sigma_{\mu_p}^2} \right\} \tag{3.28}$$

Let $\tilde{y}_p = {y_p}/{h_p^{eff}}$. Thus, $\tilde{y}_p$ can be expressed as

$$\tilde{y}_p = {y_p}/{h_p^{eff}} = s_p + {\mu_p}/{h_p^{eff}} \tag{3.29}$$

The bit metric of $c_{I,m}^p$ can finally be evaluated as

$$\begin{aligned} \wedge\left( c_{I,m}^p \right) &= \frac{1}{\sigma_{\mu_p}^2} \left\{ \min_{\varphi \in \psi_{I,m}^{(0)}} \left| y_p - h_p^{eff} \cdot \varphi \right|^2 - \min_{\varphi \in \psi_{I,m}^{(1)}} \left| y_p - h_p^{eff} \cdot \varphi \right|^2 \right\} \\ &= \frac{\left| h_p^{eff} \right|^2}{\sigma_{\mu_p}^2} \left\{ \min_{\varphi \in \psi_{I,m}^{(0)}} \left| \tilde{y}_p - \varphi \right|^2 - \min_{\varphi \in \psi_{I,m}^{(1)}} \left| \tilde{y}_p - \varphi \right|^2 \right\} \end{aligned} \tag{3.30}$$

Similar to (3.10), we can have following expression.

$$\begin{aligned} \wedge\left( c_{I,m}^p \right) &= \frac{\left| h_p^{eff} \right|^2}{\sigma_{\mu_p}^2} \left\{ \min_{\varphi \in \psi_{I,m}'^{(0)}} \left| \tilde{y}_p^I - \varphi_I \right|^2 - \min_{\varphi \in \psi_{I,m}'^{(1)}} \left| \tilde{y}_P^I - \varphi_I \right|^2 \right\} \\ &= \frac{4 \cdot \left| h_{eff}^p \right|^2}{\sigma_{\mu_p}^2} \cdot \frac{1}{4} \left\{ \min_{\varphi \in \psi_{I,m}'^{(0)}} \left| \tilde{y}_p^I - \varphi_I \right|^2 - \min_{\varphi \in \psi_{I,m}'^{(1)}} \left| \tilde{y}_p^I - \varphi_I \right|^2 \right\} \\ &= CSI \cdot D_{I,m} \end{aligned} \tag{3.31}$$

where $\tilde{y}_p^I$ represents the real part of $\tilde{y}_p$, and $\psi_{I,m}'^{(z)}$ the subset containing the real parts of the complex symbols of $\psi_{I,m}^{(z)}, z = 0,1$. Similarly, $CSI = \dfrac{4 \cdot \left| h_{eff}^p \right|^2}{\sigma_{\mu_p}^2}$ is proportional to the SNR at different sub-channel $k$. The same method simplifying

$D_{I,m}$ and $D_{Q,m}$ in SISO-OFDM system can then be applied here.

## 3.3 Optimal Receiver with LSD

With the help of the LSD detector, we can obtain the optimum soft-bit information and the performance of BICM can be enhanced. However, the price to pay is its high computational complexity. In this approach, we need a LSD detector, a vector soft-bit demapper and a soft-input Viterbi decoder. First, possible transmitted symbol vectors are detected by the LSD algorithm. Second, the soft-bit metrics are evaluated with the vector soft-bit demapper. Finally, the soft-bits are fed to the soft-input Viterbi decoder. The block diagram of the MIMO-OFDM receiver using the LSD detector for BICM decoding is shown in Fig. 3-6.

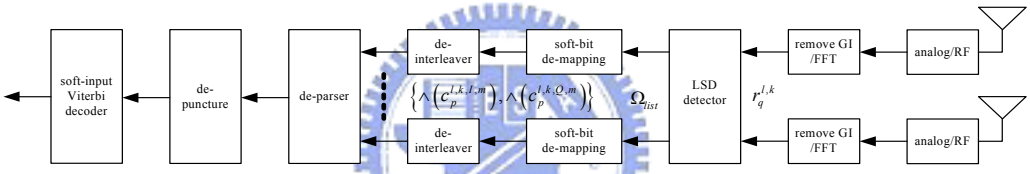


Fig. 3-6: The block diagram of the MIMO-OFDM receiver using the LSD detector for BICM

### 3.3.1 List Sphere Decoding

Since the conditional PDF of $\mathbf{r}$ obeys complex Gaussian distribution, we have

$$p\left[\mathbf{r}\middle|\mathbf{s}=\boldsymbol{\varphi}\right]=\frac{1}{\left(\pi\cdot\sigma^2\right)^{N_R}}\exp\left\{-\frac{\left|\mathbf{r}-\mathbf{H}\cdot\boldsymbol{\varphi}\right|^2}{\sigma^2}\right\} \tag{3.32}$$

where $\boldsymbol{\varphi}=\left[\varphi_1\cdots\varphi_{N_T}\right]^T$ represents the hypothesized transmitted symbol vector.

According to (3.17), $\Lambda\left(c_{I,m}^{p}\right)$ can be computed as

$$\wedge\left(c_{I,m}^{p}\right)=\frac{1}{\sigma^2}\left\{\min_{\boldsymbol{\varphi}\in\boldsymbol{\psi}_{I,m}^{(0),p}}\left|\mathbf{r}-\mathbf{H}\cdot\boldsymbol{\varphi}\right|^2-\min_{\boldsymbol{\varphi}\in\boldsymbol{\psi}_{I,m}^{(1),p}}\left|\mathbf{r}-\mathbf{H}\cdot\boldsymbol{\varphi}\right|^2\right\} \tag{3.33}$$

where $\boldsymbol{\psi}_{I,m}^{(z),p}$ represents the subset of all symbol vectors with $c_{I,m}^{p}=z, z=0,1$.

However, even with the log-sum approximation, the computational complexity grows exponentially with $N_T\cdot N_{bpsc}$, the number of transmit antennas times the number of

bits per sub-channel. So, the computational complexity of the decoding process becomes extreme high, particularly when the number of transmit antennas is large, or the QAM size is large. To find the minimum hypotheses in (3.33) for each $\Lambda\left(c_{I,m}^{p}\right)$, we need to test $2^{N_T \cdot N_{bpsc}-1}$ hypotheses in (3.33). Take the practical system of four transmitter transmit antennas and 64-QAM modulation as an example. The required number of testing approaches $2^{N_T \cdot N_{bpsc}} = 2^{24} \approx 16 \cdot 10^6$.

In [11], a scheme that can avoid the exhaustive search for maximum hypotheses was proposed. The main idea is to transform the computations in $\left|\mathbf{r}-\mathbf{H}\cdot\boldsymbol{\varphi}\right|^2$ into a tree structure and exclude the hypotheses making $\left|\mathbf{r}-\mathbf{H}\cdot\boldsymbol{\varphi}\right|^2$ large. After the detecting process is completed, the remained hypotheses, called candidate list, are used to find the two minimum terms in (3.33). Searching the candidate hypotheses in the candidate list can usually provide a good approximation to (3.33) with an appropriate list size. Using this method, the computational complexity can be effectively reduced. Then, (3.33) can be modified as

$$\wedge\left(c_{I,m}^{p}\right)=\frac{1}{\sigma^2}\left\{\min_{\boldsymbol{\varphi}\in\Omega_{list}\cap\boldsymbol{\psi}_{I,m}^{(0),p}}\left|\mathbf{r}-\mathbf{H}\cdot\boldsymbol{\varphi}\right|^2-\min_{\boldsymbol{\varphi}\in\Omega_{list}\cap\boldsymbol{\psi}_{I,m}^{(1),p}}\left|\mathbf{r}-\mathbf{H}\cdot\boldsymbol{\varphi}\right|^2\right\} \tag{3.34}$$

where $\Omega_{list}$ represents the subset of all candidate hypotheses in the candidate list.

Observe that

$$\left|\mathbf{r}-\mathbf{H}\cdot\boldsymbol{\varphi}\right|^2=\left(\boldsymbol{\varphi}-\mathbf{y}\right)^H\cdot\mathbf{H}^H\cdot\mathbf{H}\cdot\left(\boldsymbol{\varphi}-\mathbf{y}\right)+\mathbf{r}^H\cdot\left(\mathbf{I}-\mathbf{H}\cdot\left(\mathbf{H}^H\cdot\mathbf{H}\right)^{-1}\cdot\mathbf{H}^H\right)\cdot\mathbf{r} \tag{3.35}$$

where $\mathbf{y}$ is the equalized signal vector in (3.18). The ML detection for $\boldsymbol{\varphi}$ is

$$\boldsymbol{\varphi}^{ML}=\arg\min_{\boldsymbol{\varphi}\in\boldsymbol{\psi}}\left|\mathbf{r}-\mathbf{H}\cdot\boldsymbol{\varphi}\right|^2=\arg\min_{\boldsymbol{\varphi}\in\boldsymbol{\psi}}\left(\boldsymbol{\varphi}-\mathbf{y}\right)^H\cdot\mathbf{H}^H\cdot\mathbf{H}\cdot\left(\boldsymbol{\varphi}-\mathbf{y}\right) \tag{3.36}$$

where $\boldsymbol{\psi}=\left[\psi_1\cdots\psi_{N_T}\right]^T$ represents the subset of all possible symbol vectors from the constellation map. The LSD detector does not conduct an exhaustive search and only checks those points that lie inside a sphere with the given radius $r_{LSD}$ shown in Fig.

3-7, which is large enough to enclose $\boldsymbol{\varphi}^{ML}$.

$$\min_{\boldsymbol{\varphi}\in\Psi}(\boldsymbol{\varphi}-\mathbf{y})^H\cdot\mathbf{H}^H\cdot\mathbf{H}\cdot(\boldsymbol{\varphi}-\mathbf{y})\le {r_{LSD}}^2 \tag{3.37}$$

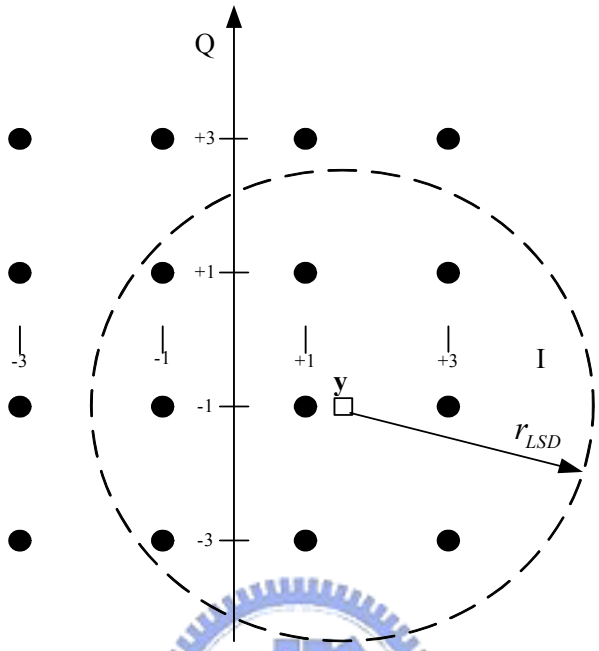


Fig. 3-7: LSD with the given radius of the sphere

We now show how to implement this idea. Let $\mathbf{U}$ be an upper triangular matrix.

Applying the cholesky factorization, we first factorize $\mathbf{H}$.

$$\mathbf{U}^H\cdot\mathbf{U}=\mathbf{H}^H\cdot\mathbf{H} \tag{3.38}$$

where

$$\mathbf{U}=\begin{bmatrix} u_{1,1} & \cdots & u_{1,N_t} \\ \vdots & u_{i,i} & \vdots \\ o & \cdots & u_{N_t,N_t} \end{bmatrix} \tag{3.39}$$

It can be proved that $u_{i,i}$ is real and positive. Then, (3.37) can be modified as

$$\begin{aligned} &(\boldsymbol{\varphi}-\mathbf{y})^H\cdot\mathbf{U}^H\cdot\mathbf{U}\cdot(\boldsymbol{\varphi}-\mathbf{y})\le {r_{LSD}}^2 \\ &\Rightarrow\sum_{i=1}^{N_t}(u_{i,i})^2\cdot\left|\varphi_i-y_i+\sum_{j=i+1}^{N_t}\frac{u_{i,j}}{u_{i,i}}\cdot(\varphi_j-y_j)\right|^2\le {r_{LSD}}^2 \end{aligned} \tag{3.40}$$

Each term in the summation over $i$ is nonnegative, and the LSD algorithm will build

different bounds on $\varphi_{N_T} \cdots \varphi_1$ step by step. With these bounds, unlikely candidates are eliminated in (3.40).

The dimension of the LSD detector is defined as $N_T$ since there are $N_T$ elements inside each candidate hypothesis. Then, the decoding process of LSD can be described as following steps.

(a). Start the process with $i = N_T$ and do not consider the rest terms, $i = 1 \cdots N_T - 1$, in (3.40). Then, (3.40) can be modified as

$$\begin{aligned} & u_{N_T,N_T}^2 \cdot \left| \varphi_{N_T} - y_{N_T} \right|^2 \le {r_{LSD}}^2 \\ & \Rightarrow \left| \varphi_{N_T} - y_{N_T} \right| \le \frac{r_{LSD}}{u_{N_T,N_T}} \end{aligned} \tag{3.41}$$

LSD will choose all possible values for $\varphi_{N_T}$ satisfying (3.41) from the constellation map.

(b). If there is no possible value for $\varphi_{N_T}$, go back to (a) and enlarge the radius of the sphere. Or, choose one of the possible values for $\varphi_{N_T}$ and go to next step where $i = N_T - 1$. Then, (3.40) can be modified as

$$u_{N_T,N_T}^2 \cdot \left| \varphi_{N_T} - y_{N_T} \right|^2 + u_{N_T-1,N_T-1}^2 \cdot \left| \varphi_{N_T-1} - y_{N_T-1} + \frac{u_{N_T-1,N_T}}{u_{N_T-1,N_T-1}} \cdot \left( \varphi_{N_T} - y_{N_T} \right) \right|^2 \le {r_{LSD}}^2$$

$$\Rightarrow \left| \varphi_{N_T-1} - y_{N_T-1} + \frac{u_{N_T-1,N_T}}{u_{N_T-1,N_T-1}} \cdot \left( \varphi_{N_T} - y_{N_T} \right) \right|^2 \le \frac{{r_{LSD}}^2 - u_{N_T,N_T}^2 \cdot \left| \varphi_{N_T} - y_{N_T} \right|^2}{u_{N_T-1,N_T-1}^2}$$

(3.42)

LSD will choose all possible values for $\varphi^{N_T-1}$ satisfying (3.42) from the constellation map.

(c). If there is no possible value for $\varphi_{N_T-1}$, go back to (b) and choose another possible value for $\varphi_{N_T}$, and a new subset of possible values for $\varphi_{N_T-1}$ will be

found. Or, choose one of the possible values for $\varphi_{N_T-1}$ and go to next step where $i = N_T - 2$. Then, (3.40) can be modified again and LSD will choose all possible values for $\varphi_{N_{T-2}}$.

(d). Use the same procedure until LSD reaches $\varphi_1$. Thus, a complete hypothesized transmitted symbol vector $\boldsymbol{\varphi} = \left[\varphi_1 \cdots \varphi_{N_T}\right]^T$ can be added into the candidate list. If there is no other possible value for $\varphi_2$, go back and try another possible value for $\varphi_3$. Then, a new subset of all possible values for $\varphi_2$ will be found. Or, choose another possible value for $\varphi_2$ and modify (3.40) again. Then, a new subset of all possible values for $\varphi_1$ will be found. The same procedure can be repeated again and again until all candidate hypotheses inside the sphere are added into the candidate list.

### 3.3.2 Real-Valued LSD

Since that QAM constellation is used, the real and imaginary parts of $\mathbf{r}$ can be decoupled. Similarly, $\mathbf{H}$ and $\boldsymbol{\varphi}$ can also be decoupled, and the original complex-valued LSD can be transferred to a real-valued LSD with the dimension of $2 \cdot N_T$ (since there are $2 \cdot N_T$ elements inside each candidate hypothesis now). Then, the object function can be modified from (3.37) as

$$\min_{\boldsymbol{\varphi}' \in \boldsymbol{\Psi}'} \left(\boldsymbol{\varphi}' - \mathbf{y}'\right)^H \cdot \mathbf{H}'^H \cdot \mathbf{H}' \cdot \left(\boldsymbol{\varphi}' - \mathbf{y}'\right) \le {r_{LSD}}^2 \tag{3.43}$$

where

$$\begin{aligned} \mathbf{y}' &= \left[\mathrm{Re}\left\{\mathbf{y}^T\right\}, \mathrm{Im}\left\{\mathbf{y}^T\right\}\right]^T \\ \boldsymbol{\varphi}' &= \left[\mathrm{Re}\left\{\boldsymbol{\varphi}^T\right\}, \mathrm{Im}\left\{\boldsymbol{\varphi}^T\right\}\right]^T \\ \mathbf{H}' &= \begin{bmatrix} \mathrm{Re}\{\mathbf{H}\} & -\mathrm{Im}\{\mathbf{H}\} \\ \mathrm{Im}\{\mathbf{H}\} & \mathrm{Re}\{\mathbf{H}\} \end{bmatrix} \end{aligned} \tag{3.44}$$

Decoding process of the real-valued LSD is simpler than the complex-valued LSD

since more candidates will be eliminated in earlier stages. However, the latency of the real-valued LSD becomes longer due to the higher dimension.

### 3.3.3 Choosing the Radius of Sphere for LSD

The size of the candidate list determines how well (3.34) can approximate (3.33). If the radius is too small, no candidate can be found. If the radius is too large, the number of candidates will be large and the required computational complexity is high. Let the true transmitted signal vector as $\boldsymbol{\varphi}^{true}$. Then,

$$\left|\mathbf{r}-\mathbf{H}\cdot\boldsymbol{\varphi}^{true}\right|^2=\left|\mathbf{n}\right|^2\sim\sigma^2\cdot\chi^2_{N_T} \tag{3.45}$$

where $\chi^2_{N_T}$ is a random variable having a chi-square distribution with $N_T$ degrees of freedom. The expected value of the sum of the squared noise is $\sigma^2\cdot E\left\{\chi^2_{N_T}\right\}=\sigma^2\cdot N_T$. So, we can choose the radius of the sphere as

$$\begin{aligned} r_{LSD}{}^2 &= \sigma^2\cdot C_{LSD}\cdot N_T-\mathbf{r}^H\cdot\left(\mathbf{I}-\mathbf{H}\cdot\left(\mathbf{H}^H\cdot\mathbf{H}\right)^{-1}\cdot\mathbf{H}^H\right)\cdot\mathbf{r} \\ &\approx \sigma^2\cdot C_{LSD}\cdot N_T \end{aligned} \tag{3.46}$$

where $C_{LSD}$ represents a real-valued constant that is greater than 1. When a suitable value for $C_{LSD}$, evaluated by a confidence interval for $\chi^2_{N_T}$, is determined, the radius of the sphere can be determined. However, for a suitable $C_{LSD}$, there will be some cases that no candidate hypothesis can be found. In these cases, the radius of the sphere needed to be enlarged until $\Omega_{list}\cap\boldsymbol{\psi}^{(0),p}_{I,m}\neq empty$ or $\Omega_{list}\cap\boldsymbol{\psi}^{(1),p}_{I,m}\neq empty$. If $\Omega_{list}\cap\boldsymbol{\psi}^{(0),p}_{I,m}\neq empty$ but $\Omega_{list}\cap\boldsymbol{\psi}^{(1),p}_{I,m}=empty$, the second term in (3.34) can be replaced by a real-valued constant greater than $r_{LSD}{}^2$. If $\Omega_{list}\cap\boldsymbol{\psi}^{(1),p}_{I,m}\neq empty$ but $\Omega_{list}\cap\boldsymbol{\psi}^{(0),p}_{I,m}=empty$, the first term in (3.34) can be replaced by a real-valued constant greater than $r_{LSD}{}^2$. This is to make assure that each $\wedge\left(c^p_{I,m}\right)$ can be calculated.

## 3.4 Simulation Results

As mentioned, our simulation platform is developed based on the 802.11n TGn Sync proposal. We use the mandatory mode in which the constraint length for the convolutional code is 7, the channelization bandwidth is 20MHz (56 occupied sub-channels), and the number of spatial streams is two ( $N_T = 2$ ). The number of receive antennas is the same as that of transmit antennas. A MMSE equalizer and a simplified soft-bit demapper are used at the receiver. A soft-input Viterbi decoder with trace back length of 128 is used to detect information bits. Assume that the frequency offset and timing offset are perfectly compensated at the receiver. We use the HT-LTF of the preamble and the standard per-tone channel estimation method (no smoothing) to estimate MIMO channels. PPDU length is set as 1000 bytes; so there are 8000 information bits in each package. The packet error rate (PER) is used as the performance measure. We compare our simulation results with those reported in [16] for CC59 (CC59 is a specific parameter setting environment in [20]). From Fig. 3-8, we can see that our simulation results match those in [16] quite well. Note that the channel used here is AWGN.

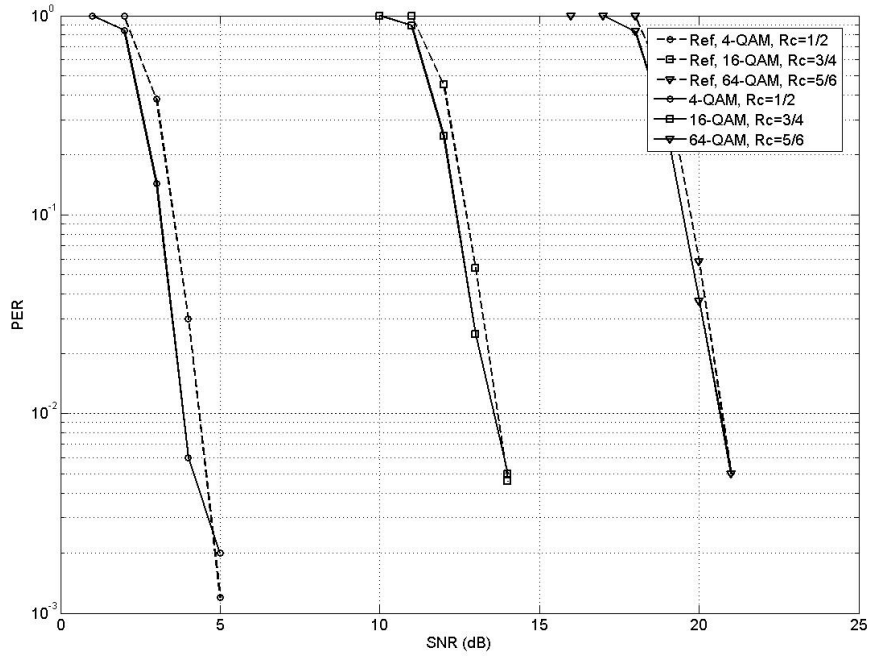


Fig. 3-8: Performance comparison (BICM, 20MHz, 2x2, AWGN-channel)

Fig. 3-9 to Fig. 3-11 show simulation results for another scenario, which is called CC67 PHY-2. Here, CC67 represents a specific parameter setting environment in [20], and PHY-2 represents a specific task group. From these figures, we can see that our simulation results match those in [16] well (channel-B, channel-D and channel-E).

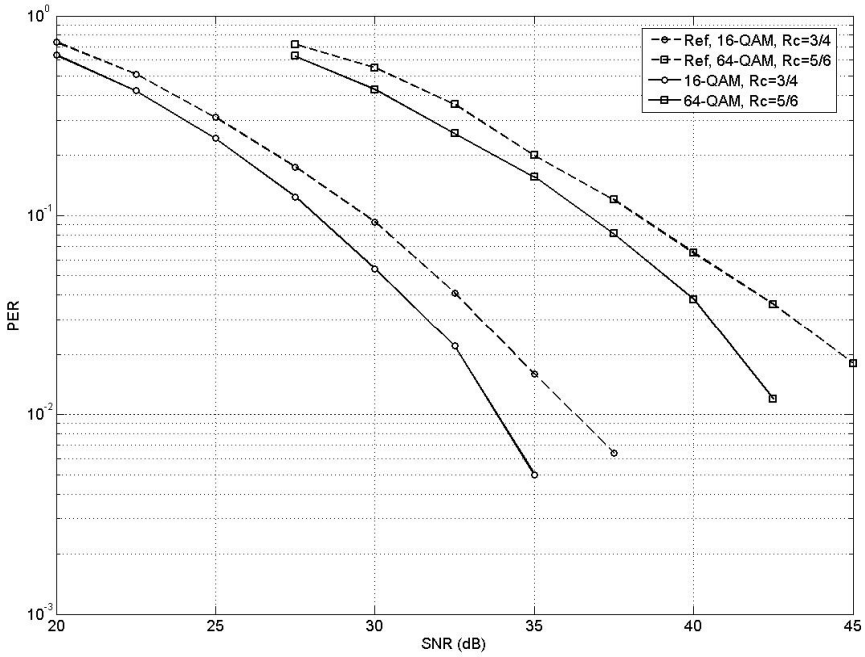


Fig. 3-9: Performance comparison of BICM-EQL (20MHz, 2x2, channel-B)

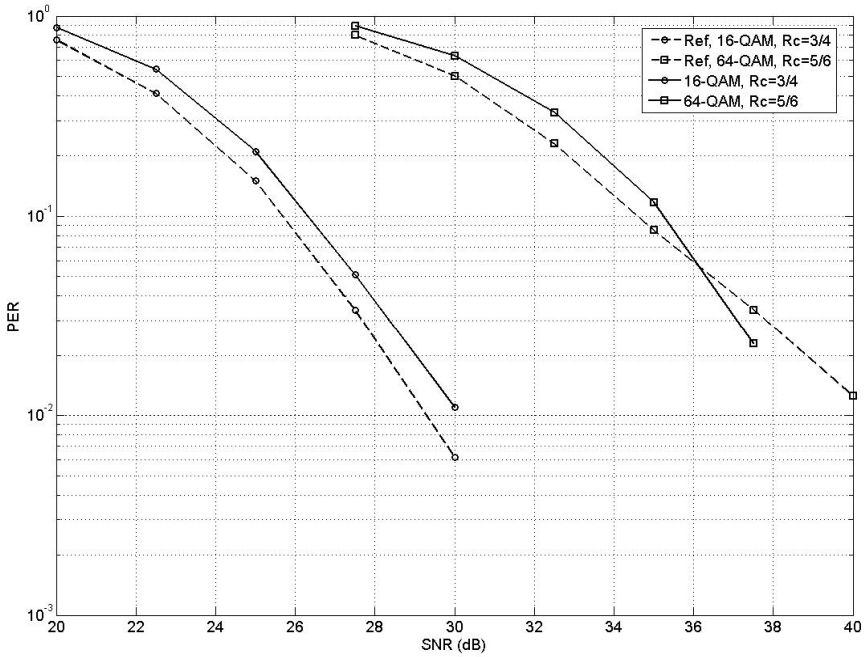


Fig. 3-10: Performance comparison of BICM-EQL (BICM, 20MHz, 2x2, channel-D)

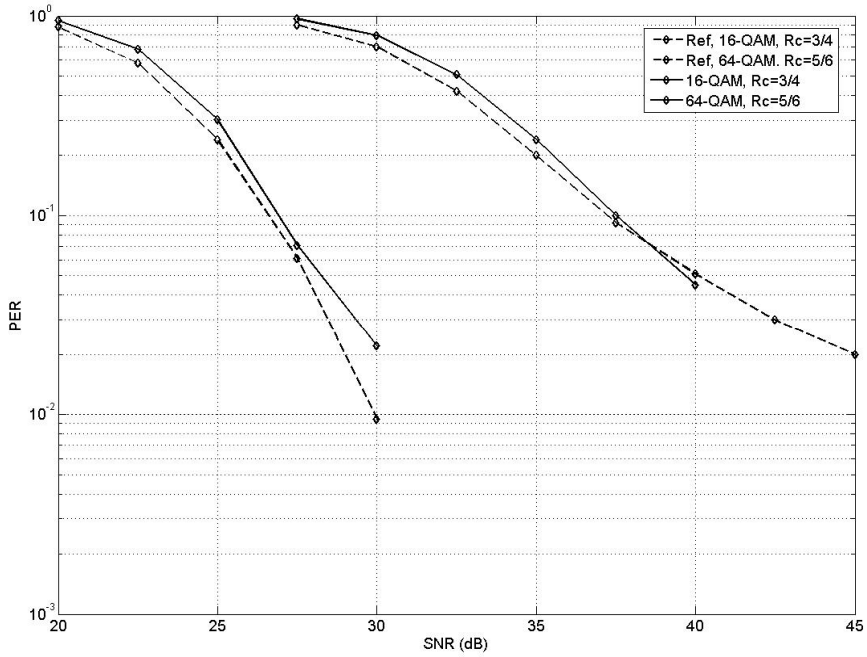


Fig. 3-11: Performance comparison of BICM-EQL (BICM, 20MHz, 2x2, channel-E)

# Chapter 4 MIMO-OFDM with TICM

Although the LSD detector can reduce the complexity of optimum soft-bit demapper, the computational complexity still grows with $N_T \cdot N_{bpsc}$. Besides, a memory with the size of $2^{N_T \cdot N_{bpsc}}$ is required to save the candidate list. This is for the worst case that all possible symbol vectors are included inside the sphere of the LSD. So, the decoding process is still complicated and the required memory size is large. This is particularly true when the number of multiple transmit antennas is large, or the QAM size is large.

To solve above problems, we propose a new coding and modulation scheme, called TICM, for MIMO-OFDM systems. The main difference between BICM and TICM lies in the level of interleaving. The interleaver at the BICM transmitter uses a bit as its basic unit while the interleaver at the TICM transmitter uses a block of $N_T$ symbols as its basic unit. This results in different decoding architectures at the receiver. The main advantage of TICM is to merge soft-bit demapping into the Viterbi algorithm. Taking the advantage of the trellis structure inherent in the Viterbi algorithm, TICM can have lower computational complexity and potentially better performance than BICM with the LSD soft-bit demapping. Although the tone-level interleaving may not have spatial diversity gain, the performance is not affected in 802.11n environments.

### 4.1.1 Transmitter

Information bits are first encoded by the FEC encoder, and the resultant coded bits are then mapped to symbols consecutively. The row-input-column-output tone-level interleaver uses $\mathbf{s}^j = \left[ s_1^j, \cdots, s_{N_T}^j \right]$, the $j^{th}$ block of $N_T$ modulated symbols, mapped from $N_T \cdot N_{bpsc}$ coded bits, as its basic unit to perform interleaving.

The index $j$ starts from "1" to "$L_s \cdot K$", where $L_s$ represents the number of OFDM symbols per transmit antenna, and $K$ the number of OFDM sub-channels. Thus, there are total $L_s \cdot K$ blocks at each transmission package. For the moment, we will not consider puncturing in TICM. Then, the parser will parse $\mathbf{s}^{l,k}$ to each corresponding antenna, where $l$ represents the index of the modulated symbol sequence, and $k$ the index of the sub-channel. The remained transmission process is the same with the BICM. The block diagram of the TICM transmitter is shown in Fig. 4-1.

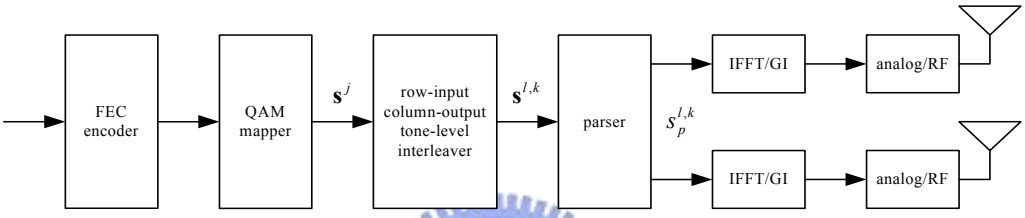


Fig. 4-1: The block diagram of the MIMO-OFDM transmitter for TICM

Take a CC encoder shown in Fig. 4-2 as an example. Here, $K_{CC} = 3$ and $R_c = 1/2$, where $K_{CC}$ represents the constraint length and $R_c$ the coding rate. We also assume that four transmit antennas and 16-QAM modulation are used at the transmitter.

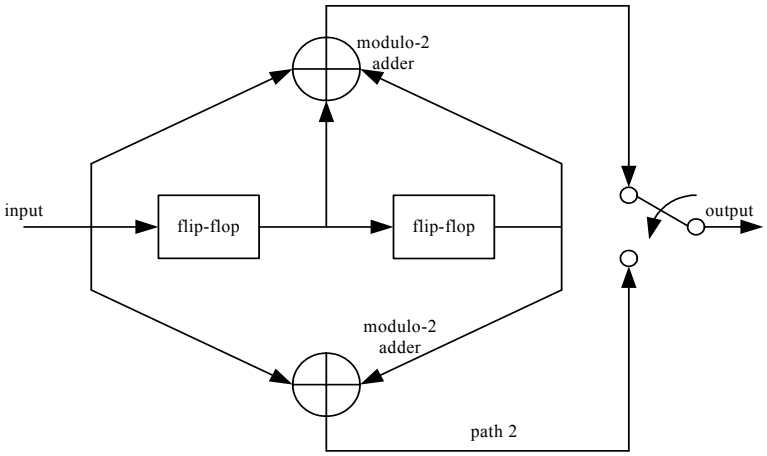


Fig. 4-2: The CC encoder with $K_{CC} = 3$

Encoding process of the CC encoder can be explained in the trellis diagram shown in

Fig. 4-3. For the case considered here, there are $2^{K_{CC}-1}=4$ possible states. Each state has two incoming and two outgoing branches. A transition from one state to another in response to input "0" is represented by a solid line and that in response to input "1" is represented by a dashed line. The binary number labeled on each branch represents the output of the encoder as it moves from one state to another. Since a block of four modulated symbols are mapped from a consecutive sixteen output of the encoder, we define one stage in the trellis diagram as eight continuous time instants in the trellis diagram. Each stage is also a basic unit in the decoding process at the receiver, which is similar to a radix-$2^8$ Viterbi structure.

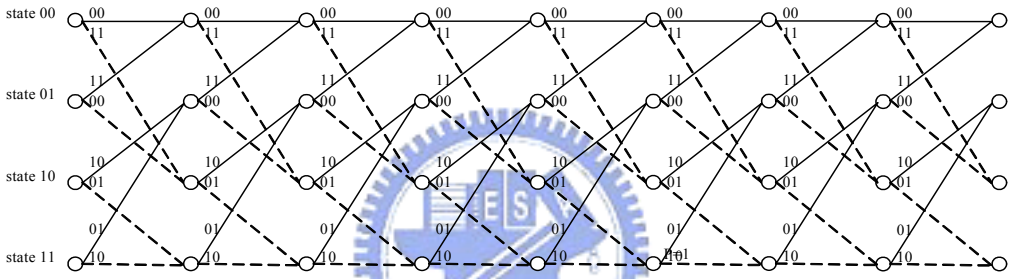


Fig. 4-3: The trellis diagram at the $j^{th}$ stage for the CC encoder

Fig. 4-3 can be re-drawn as that in Fig. 4-4 if each two consecutive time instants are merged into one. So each new branch is corresponding to one of four possible input sequences, "00", "01", "10" and "11". The decimal number, transformed from the binary number, labeled on each branch, represents the output of the encoder as it moves from one state to another. Now, each time instant in the trellis outputs a 16-QAM symbol.

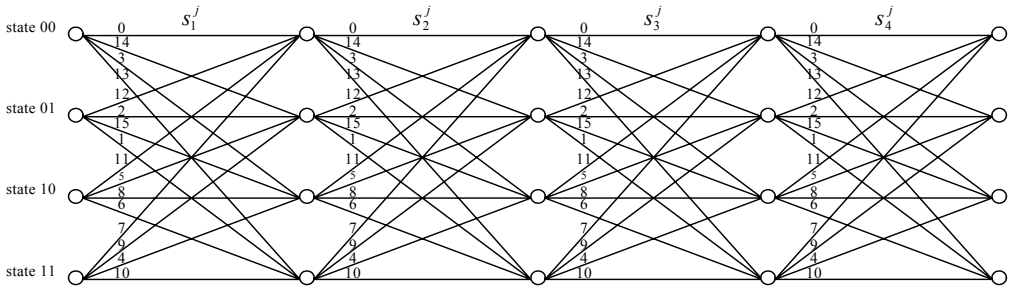

Fig. 4-4: The modified trellis diagram at the $j^{th}$ stage for the CC encoder

Observed from Fig. 4-4, $\mathbf{s}^j = \left[ s_1^j, \cdots, s_4^j \right]$ represents the outputs of the encoder at the $j^{th}$ stage through the trellis diagram (four transmit antennas). Take a hypothesized legal path starting from the first state at the $j^{th}$ stage as an example, its corresponding output bits are assumed to be {1110, 1100, 1101, 0111}. From Fig. 4-4, the output bits can be represented as {14, 12, 13, 7}, which indicates $\left[ s_1^j, s_2^j, s_3^j, s_4^j \right] = [14,12,13,7]$. Then, the tone-level interleaver uses a block of four symbols as its basic unit for interleaving. Finally, the parser will parse each of these four symbols to their corresponding transmit antennas.

### 4.1.2 Receiver

In BICM, soft-bit values are first computed, and these values are then used in the Viterbi decoder to calculate the BMs. In TICM, the BMs can be directly computed without involving the soft-bit demapper. First, the received symbol blocks $\mathbf{r}^{l,k}$ are de-interleaved. Second, the BMs are evaluated with the estimated MIMO channel and the trellis diagram in Fig. 4-4. As mentioned, the whole trellis in Fig. 4-4 corresponds to one stage. This is also equivalent to describe this structure as a parallel transition. Finally, the BMs are feed into the soft-input Viterbi decoder. The block diagram of the receiver for the MIMO-OFDM system with TICM is shown in Fig. 4-5. The detailed decoding procedure is described in the next subsection.

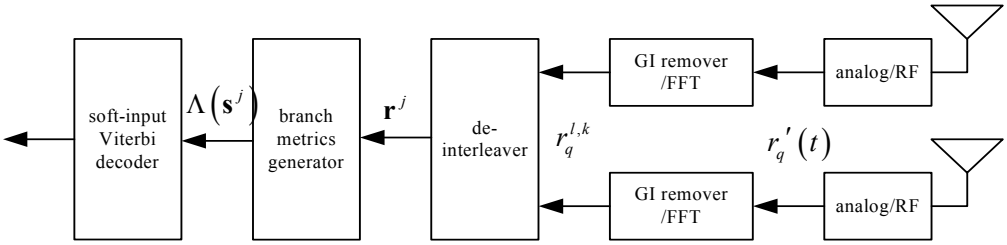


Fig. 4-5: The block diagram of the MIMO-OFDM receiver for TICM

### 4.1.3 Modified Soft-Input Viterbi Decoder

The output symbols corresponding to the maximum likelihood path through the trellis diagram can be expressed as

$$\boldsymbol{\varphi}^{ML-path} = \arg\max_{\boldsymbol{\varphi}^{trel,j} \in \boldsymbol{\psi}^{trel,j}} p\left[\left[\mathbf{r}^1,\cdots,\mathbf{r}^j,\cdots,\mathbf{r}^{L_s\cdot K}\right] \middle| \left[\mathbf{s}^1,\cdots,\mathbf{s}^j,\cdots,\mathbf{s}^{L_s\cdot K}\right] = \left[\boldsymbol{\varphi}^{trel,1},\cdots,\boldsymbol{\varphi}^{trel,j},\cdots,\boldsymbol{\varphi}^{trel,L_s\cdot K}\right]\right] \tag{4.1}$$

where $\boldsymbol{\varphi}^{trel,j}$ represents the output symbols corresponding to the hypothesized legal path at the $j^{th}$ stage (in the trellis diagram), and $\boldsymbol{\psi}^{trel,j}$ the subset of the output symbols corresponding to all legal paths at the $j^{th}$ stage. Assume that the channel is memoryless (this is true in OFDM). (4.1) can be rewritten as

$$\begin{aligned} & p\left[\left[\mathbf{r}^1,\cdots,\mathbf{r}^j,\cdots,\mathbf{r}^{L_s\cdot K}\right] \middle| \left[\mathbf{s}^1,\cdots,\mathbf{s}^j,\cdots,\mathbf{s}^{L_s\cdot K}\right] = \left[\boldsymbol{\varphi}^{trel,1},\cdots,\boldsymbol{\varphi}^{trel,j},\cdots,\boldsymbol{\varphi}^{trel,L_s\cdot K}\right]\right] \\ & = \prod_{j=1}^{L_s\cdot K} p\left[\mathbf{r}^j \middle| \mathbf{s}^j = \boldsymbol{\varphi}^{trel,j}\right] \end{aligned} \tag{4.2}$$

where $\mathbf{r}^j$ represents the de-interleaved symbol block. Since the conditional PDF of $\mathbf{r}^j$ obeys complex Gaussian distribution.

$$p\left[\mathbf{r}^j \middle| \mathbf{s}^j = \boldsymbol{\varphi}^{trel,j}\right] = \frac{1}{\left(\pi\cdot\sigma^2\right)^{N_R}} \exp\left\{-\frac{\left|\mathbf{r}^j - \mathbf{H}^j\cdot\boldsymbol{\varphi}^{trel,j}\right|^2}{\sigma^2}\right\} \tag{4.3}$$

where $\mathbf{H}^j$ represents the MIMO-channel after de-interleaveing. We define the log-likelihood function of (4.1) as

$$\begin{aligned} \boldsymbol{\varphi}^{ML-path} &= \arg\max_{\boldsymbol{\varphi}^{trel,j} \in \boldsymbol{\psi}^{trel,j}} \ln\left(\prod_{j=1}^{L_s\cdot K} p\left[\mathbf{r}^j \middle| \mathbf{s}^j = \boldsymbol{\varphi}^{trel,j}\right]\right) \\ &= \arg\max_{\boldsymbol{\varphi}^{trel,j} \in \boldsymbol{\psi}^{trel,j}} \sum_{j=1}^{L_s\cdot K} \ln\left(p\left[\mathbf{r}^j \middle| \mathbf{s}^j = \boldsymbol{\varphi}^{trel,j}\right]\right) \\ &= \arg\max_{\boldsymbol{\varphi}^{trel,j} \in \boldsymbol{\psi}^{trel,j}} \sum_{j=1}^{L_s\cdot K} \left(-\left|\mathbf{r}^j - \mathbf{H}^j\cdot\boldsymbol{\varphi}^{trel,j}\right|^2\right) \end{aligned} \tag{4.4}$$

Let $N_{ibps} = N_T \cdot N_{bpsc} \cdot R_c$ be the number of information bits in each stage. Thus,

finding the maximum likelihood path needs to examine $2^{K_{CC}-1}\cdot\left(2^{N_{ibps}}\right)^{L_s\cdot K}$ paths through the trellis diagram, where $2^{K_{CC}-1}$ represents the number of beginning states in the trellis diagram. Here we can use the Viterbi algorithm [12] to reduce the complexity. Note that the total trellis stages are $L_s\cdot K$. We define the BM of $\mathbf{s}^j$ at the $j^{th}$ stage for TICM as

$$\Lambda\left(\mathbf{s}^j\right)=-\left|\mathbf{r}^j-\mathbf{H}^j\cdot\boldsymbol{\varphi}^{trel,j}\right|^2 \tag{4.5}$$

So, finding $\boldsymbol{\varphi}^{ML-path}$ can be rewritten as

$$\boldsymbol{\varphi}^{ML-path}=\underset{\boldsymbol{\varphi}^{trel,j}\in\boldsymbol{\psi}^{trel,j}}{\arg\max}\sum_{j=1}^{L_s\cdot K}\Lambda\left(\mathbf{s}^j\right) \tag{4.6}$$

Then, define the $i^{th}$ state metric at the $j^{th}$ stage for TICM as

$$M_i\left(j\right), i\in\left\{1,\cdots,2^{K_{CC}-1}\right\}. \tag{4.7}$$

The state metric indicates the greatest accumulated BMs among all legal paths from the first stage to the $j^{th}$ stage merging to the $i^{th}$ state. Thus, we can have the recursive equation for state metric as

$$M_i\left(j+1\right)=\max_{i'\in I}\left\{M_{i'}\left(j\right)+\Lambda_{i',i}\left(\mathbf{s}^j\right)\right\} \tag{4.8}$$

where $\Lambda_{i',i}\left(\mathbf{s}_j\right)$ represents the BM over the transition branch form the $i'^{th}$ state to the $i^{th}$ state at the $j^{th}$ stage, and $I$ represents the subset of all states having permissible transition from the previous stage to the $i^{th}$ state at the $j^{th}$ stage. To compute the state metric, the Viterbi algorithm involves an add-compare-select (ACS) operation. The detailed operation is explained below.

(a). Add: Add new BM to the previous state metric for each path merging to the state.

(b). Compare: Compare the total metric of different paths merging to the state.

(c). Select: Select the path with the greatest metric merging to the state and record both the updated state metric and the survived path.

After $M_i\left(L_s \cdot K+1\right)$ is evaluated at the $\left(L_s \cdot K\right)^{th}$ stage, the state with the greatest state metric is then selected. Then, the survived path is then traced back, from the last stage to the first stage. Each detected branch at the $j^{th}$ stage will then output $N_{ibps}$ information bits. This procedure is called chaining (trace) back. After chaining back, the decoding process is completed.

There are two commonly used methods, called tailing off and memory truncation, to simplify the Viterbi decoder commonly. Insert a zero sequence whose length is $K_{CC}-1$ at the end of the information bit sequence to force the CC encoder to return to its initial all-zero state. This procedure is called tailing off. In the original decoding process, the survived path recorded at each stage is stored in the path memory until the chaining back procedure starts. So, the storage requirement for the Viterbi decoder becomes very high when $L_s \cdot K$ is long. With little performance degradation, we may chain back from the state with the greatest state metric for a sufficient converging length, called trace back length. Usually five times of the constraint length is enough for good performance. Once the decisive bits that we have chained back are decoded out and the recorded survived branch can be deleted from the path memory. This process is called memory truncation.

## 4.2 Suboptimal Receiver

Observing (4.5), we find that there are $2^{K_{CC}-1} \cdot 2^{N_{ibps}}$ legal paths though the trellis diagram at the $j^{th}$ stage. In other words, the complexity for evaluating the BM of $\Lambda\left(\mathbf{s}^j\right)$, grows exponentially with $K_{CC}+N_{ibps}$, the constraint length and the number of information bits per stage. Obviously, direct implementation of (4.5) may not be feasible. Note that $2^{K_{CC}-1}$ corresponds to the number of beginning states at the $j^{th}$ stage, and $2^{N_{ibps}}$ corresponds to the number of all legal paths starting from

each beginning state. In the following subsections, we will propose suboptimal approaches to reduce the computational complexity. The first one is to reduce the number of the beginning states, and the second one is to reduce the number of legal paths being searched.

### 4.2.1 Suboptimal Receiver with State Reduction

Since that the BM at each stage in TICM corresponds to a block of $N_T$ symbols, information embedded in the BM is higher than that in BICM (only one bit). Thus, the state metrics in TICM provide more reliable information than that in BICM. Define the subset of beginning states with the greatest $C_{SMI}$ state metrics as $I_{SMI}$, where $1 \le C_{SMI} \le 2^{K_{CC}-1}$. With predictable performance degradation, we can only consider the paths beginning from $I_{SMI}$ and eliminate others. Define the $i^{th}$ state belonging to $I_{SMI}$ as $i_{SMI}$, and the BM of $\mathbf{s}^j$, starting from the $i_{SMI}^{th}$ state and merging to the $i^{th}$ state at the $j^{th}$ stage, as $\Lambda_{i_{SMI},i}\left(\mathbf{s}^j\right)$. Then, the recursive equation in (4.8) can be modified as

$$M_i\left(j+1\right) = \max_{i_{SMI} \in I_{SMI}} \left\{ M_{i_{SMI}}\left(j\right) + \Lambda_{i_{SMI},i}\left(\mathbf{s}^j\right) \right\} \tag{4.9}$$

This suboptimal decoding method is almost the same with what we mentioned in 4.1.3. However, the complexity of the BM evaluation is reduced to a factor of $C_{MSI}/2^{K_{CC}-1}$.

We now use the receiver in the example in 4.1.1 as an illustration example. Let $C_{SMI} = 2$. At the $j^{th}$ decoding stage, suppose that the first and third state have the greatest two state metrics. Then, we only have to evaluate $\Lambda_{1,i}\left(\mathbf{s}^j\right)$ and $\Lambda_{3,i}\left(\mathbf{s}^j\right)$, where $i \in \{1,2,3,4\}$. Finally, the ACS module will determine the survived branch. The modified trellis diagram at the $j^{th}$ stage is shown in Fig. 4-6.

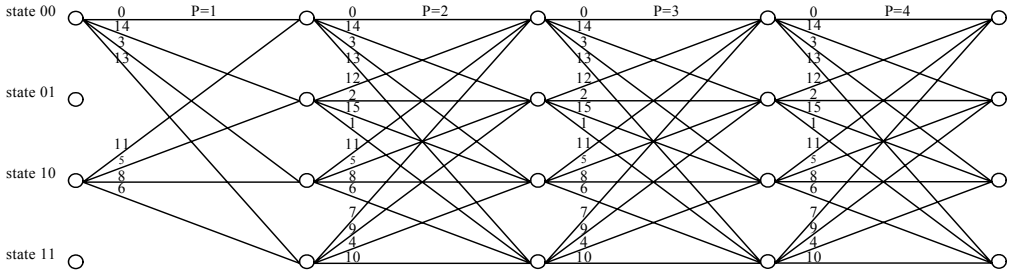


Fig. 4-6: The modified trellis diagram at the $j^{th}$ stage with SMI

Note that $C_{MSI}$ determines how well (4.9) can approximate (4.8). So, there is a trade off between the computational complexity and performance degradation. The block diagram of this suboptimal MIMO-OFDM receiver is shown in Fig. 4-7.

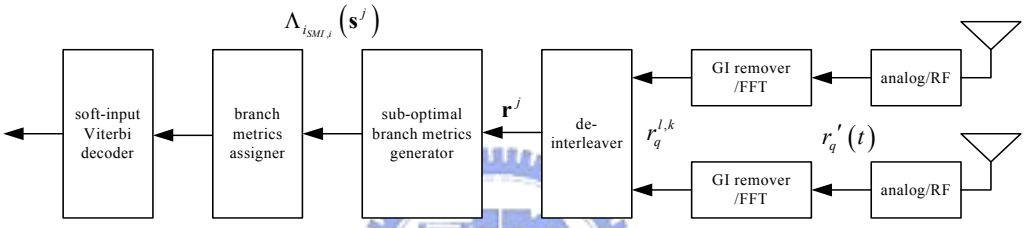


Fig. 4-7: The block diagram of the MIMO-OFDM receiver using SMI for TICM

### 4.2.2 Suboptimal Receiver with LSD

Even we have reduced the number of the beginning states, there are still $2^{N_{ibps}}$ legal paths for each beginning state. The computational complexity for evaluating $\Lambda_{i_{SMI,j}}(\mathbf{s}^j)$ still grows exponentially with $N_{ibps}$. Observe (4.5), we can find that the BM calculation problem is an ML problem. Thus, we can extend the use of the LSD detector to reduce the computational complexity of the BM calculation. With a tree structure formulation, we can exclude the symbols corresponding to the hypothesized legal paths making $\left|\mathbf{r}^j - \mathbf{H}^j \cdot \boldsymbol{\varphi}^{trel,j}\right|^2$ large. In this way, we can search for the legal paths that maximize the term in (4.9). With a suitable number of candidate paths, maximization of (4.9) can be well approximated. Define the subset of the symbol sequences corresponding to the candidate paths as candidate path list, $\Omega_{list}^{trel}$. Note that the legal paths in the LSD detector here ($2^{N_{ibsc}}$) is much smaller than those in BICM

( $2^{N_T N_{bpsc}}$ ). This is due to the trellis structure we have here. So, the BM of $\mathbf{s}^j$ that begins from the $i_{SMI}^{th}$ state at the $j^{th}$ stage within $\Omega_{list}^{trel}$ can be expressed as

$$\Lambda_{i_{SMI}}^{\Omega}\left(\mathbf{s}^j\right) = -\left|\mathbf{r}^j - \mathbf{H}^j \cdot \boldsymbol{\varphi}^{trel,j}\right|^2 \tag{4.10}$$

where $\boldsymbol{\varphi}^{trel,j} \in \boldsymbol{\psi}^{trel,j} \cap \Omega_{list}^{trel}$, and $\boldsymbol{\varphi}^{trel,j} = \left[\varphi_1^{trel,j}, \cdots, \varphi_{N_T}^{trel,j}\right]^T$ represents the output symbols corresponding to the hypothesized legal path starting from the $i_{SMI}^{th}$ state, and $\boldsymbol{\psi}^{trel,j} = \left[\psi_1^{trel,j}, \cdots, \psi_{N_T}^{trel,j}\right]^T$ the subset of the output symbols corresponding to all legal paths that starts from the $i_{SMI}^{th}$ state. Then, (4.9) can be modified as

$$M_i\left(j+1\right) = \max_{i_{SMI} \in I_{SMI}} \left\{ M_{i_{SMI}}\left(j\right) + \Lambda_{i_{SMI},i}^{\Omega}\left(\mathbf{s}^j\right) \right\} \tag{4.11}$$

where $\Lambda_{i_{SMI},i}^{\Omega}\left(\mathbf{s}^j\right)$ represents the BM over the transition branch form the $i_{SMI}^{th}$ state to the $i^{th}$ state. Thus, to evaluate $\Lambda_{i_{SMI}}^{\Omega}\left(\mathbf{s}^j\right)$, we need a LSD detector. As a result, the number of the LSD detectors we need is $C_{SMI}$. We will show that the computational complexity can be greatly reduced with these suboptimal approaches.

In what follows, we will show how to implement the LSD detector in the BM calculation. Observe that

$$\begin{aligned}\left|\mathbf{r}^j - \mathbf{H}^j \cdot \boldsymbol{\varphi}^{trel,j}\right|^2 &= \left(\boldsymbol{\varphi}^{trel,j} - \mathbf{y}^j\right)^H \cdot \left(\mathbf{H}^j\right)^H \cdot \mathbf{H}^j \cdot \left(\boldsymbol{\varphi}^{trel,j} - \mathbf{y}^j\right) + \\ &\left(\mathbf{r}^j\right)^H \cdot \left(\mathbf{I} - \mathbf{H}^j \cdot \left(\left(\mathbf{H}^j\right)^H \cdot \mathbf{H}^j\right)^{-1} \cdot \left(\mathbf{H}^j\right)^H\right) \cdot \mathbf{r}^j\end{aligned} \tag{4.12}$$

where $\mathbf{y}^j$ is the equalized signal vector of $\mathbf{r}_j$ in (3.18). We will omit the index $j$ in the rest of this thesis for simplicity. (4.12) can be rewritten as

$$\begin{aligned}\left|\mathbf{r} - \mathbf{H} \cdot \boldsymbol{\varphi}^{trel}\right|^2 &= \left(\boldsymbol{\varphi}^{trel} - \mathbf{y}\right)^H \cdot \mathbf{H}^H \cdot \mathbf{H} \cdot \left(\boldsymbol{\varphi}^{trel} - \mathbf{y}\right) + \\ &\mathbf{r}^H \cdot \left(\mathbf{I} - \mathbf{H} \cdot \left(\mathbf{H}^H \cdot \mathbf{H}\right)^{-1} \cdot \mathbf{H}^H\right) \cdot \mathbf{r}\end{aligned} \tag{4.13}$$

We define a matrix with its columns reversed from $\mathbf{H}$ as

$$\bar{\mathbf{H}} = \begin{bmatrix} h_{1,N_T} & \cdots & h_{1,1} \\ \vdots & h_{q,p} & \vdots \\ h_{N_R,N_T} & \cdots & h_{N_R,1} \end{bmatrix}, \tag{4.14}$$

a vector with its elements reversed from $\mathbf{y}$ as

$$\bar{\mathbf{y}} = \left[ y_{N_T}, \cdots, y_1 \right]^T, \tag{4.15}$$

a vector with elements reversed from $\boldsymbol{\varphi}^{trel}$ as

$$\bar{\boldsymbol{\varphi}}^{trel} = \left[ \varphi_{N_T}^{trel}, \cdots, \varphi_1^{trel} \right]^T, \tag{4.16}$$

and a subset with its elements reversed from $\boldsymbol{\psi}^{trel}$ as

$$\bar{\boldsymbol{\psi}}^{trel} = \left[ \bar{\psi}_{N_T}^{trel}, \cdots, \bar{\psi}_1^{trel} \right]^T. \tag{4.17}$$

Then, (4.13) can be rewritten as

$$\begin{aligned} \left| \mathbf{r} - \mathbf{H} \cdot \boldsymbol{\varphi}^{trel} \right|^2 &= \left| \mathbf{r} - \bar{\mathbf{H}} \cdot \bar{\boldsymbol{\varphi}}^{trel} \right|^2 \\ &= \left( \bar{\boldsymbol{\varphi}}^{trel} - \bar{\mathbf{y}} \right)^H \cdot \bar{\mathbf{H}}^H \cdot \bar{\mathbf{H}} \cdot \left( \bar{\boldsymbol{\varphi}}^{trel} - \bar{\mathbf{y}} \right) + \mathbf{r}^H \cdot \left( \mathbf{I} - \bar{\mathbf{H}} \cdot \left( \bar{\mathbf{H}}^H \cdot \bar{\mathbf{H}} \right)^{-1} \cdot \bar{\mathbf{H}}^H \right) \cdot \mathbf{r} \end{aligned} \tag{4.18}$$

The LSD method only check those points that lie inside a sphere with the given radius $r_{LSD}$, which is large enough to enclose the term maximizing (4.9).

$$\min_{\bar{\boldsymbol{\varphi}}^{trel} \in \bar{\boldsymbol{\psi}}^{trel}} \left( \bar{\boldsymbol{\varphi}}^{trel} - \bar{\mathbf{y}} \right)^H \cdot \bar{\mathbf{H}}^H \cdot \bar{\mathbf{H}} \cdot \left( \bar{\boldsymbol{\varphi}}^{trel} - \bar{\mathbf{y}} \right) \le {r_{LSD}}^2 \tag{4.19}$$

Let $\mathbf{U}$ be an upper triangular matrix. We can factorize $\bar{\mathbf{H}}$ by the cholesky factorization as

$$\mathbf{U}^H \cdot \mathbf{U} = \bar{\mathbf{H}}^H \cdot \bar{\mathbf{H}} \tag{4.20}$$

where

$$\mathbf{U} = \begin{bmatrix} u_{1,1} & \cdots & u_{1,N_t} \\ \vdots & u_{i,i} & \vdots \\ o & \cdots & u_{N_t,N_t} \end{bmatrix}. \tag{4.21}$$

Note that $u_{i,i}$ can be shown to be real and positive. Then, (4.19) can be rewritten as

$$\begin{aligned}
&\left(\bar{\boldsymbol{\varphi}}^{trel}-\bar{\mathbf{y}}\right)^{H}\cdot\mathbf{U}^{H}\cdot\mathbf{U}\cdot\left(\bar{\boldsymbol{\varphi}}^{trel}-\bar{\mathbf{y}}\right)\le {r_{LSD}}^{2}\\
&\Rightarrow\sum_{i=1}^{N_t}\left(u_{i,i}\right)^{2}\cdot\left|\varphi_{N_T+1-i}^{trel}-y_{N_T+1-i}+\sum_{j=i+1}^{N_t}\frac{u_{i,j}}{u_{i,i}}\cdot\left(\varphi_{N_T+1-j}^{trel}-y_{N_T+1-j}\right)\right|^{2}\le {r_{LSD}}^{2}
\end{aligned}\tag{4.22}$$

Each term in the summation over $i$ in (4.22) is nonnegative, and the LSD method will build a tree structure. With bounds on $\varphi_1^{trel}\cdots\varphi_{N_T}^{trel}$, the LSD method can eliminate unlikely paths step by step using (4.22).

The dimension of LSD is defined as $N_T$ since there are $N_T$ elements inside each candidate hypothesis. Then, the decoding process of the LSD method, starting from the $i_{SMI}^{th}$ state (at the $j^{th}$ stage), can be summarized as follows.

(a). Start the process from $i=N_T$ and do not consider the rest terms, $i=1\cdots N_T-1$ in (4.22). Then, (4.22) becomes

$$\begin{aligned}
&u_{N_T,N_T}^{2}\cdot\left|\varphi_1^{trel}-y_1\right|^{2}\le {r_{LSD}}^{2}\\
&\Rightarrow\left|\varphi_1^{trel}-y_1\right|\le\frac{r_{LSD}}{u_{N_T,N_T}}
\end{aligned}\tag{4.23}$$

The LSD method will choose all possible values for $\varphi_1^{trel}$ satisfying (4.23) from $\psi_1^{trel}$, where $\psi_1^{trel}$ is determined by all branches starting from the $i_{SMI}^{th}$ state.

(b). If there is no possible value for $\varphi_1^{trel}$, go back to (a) and enlarge the radius of the sphere. Or, choose one of the possible values for $\varphi_1^{trel}$ and go to next step where $i=N_T-1$. Then, (4.22) becomes

$$\begin{aligned}
&u_{N_T,N_T}^{2}\cdot\left|\varphi_1^{trel}-y_1\right|^{2}+u_{N_T-1,N_T-1}^{2}\cdot\left|\varphi_2^{trel}-y_2+\frac{u_{N_T-1,N_T}}{u_{N_T-1,N_T-1}}\cdot\left(\varphi_1^{trel}-y_1\right)\right|^{2}\le {r_{LSD}}^{2}\\
&\Rightarrow\left|\varphi_2^{trel}-y_2+\frac{u_{N_T-1,N_T}}{u_{N_T-1,N_T-1}}\cdot\left(\varphi_1^{trel}-y_1\right)\right|^{2}\le\frac{{r_{LSD}}^{2}-u_{N_T,N_T}^{2}\cdot\left|\varphi_1^{trel}-y_1\right|^{2}}{u_{N_T-1,N_T-1}^{2}}
\end{aligned}\tag{4.24}$$

LSD will choose all possible values for $\varphi_2^{trel}$ satisfying (4.24) from $\psi_2^{trel}$, where

$\psi_2^{trel}$ is determined by the state that $\varphi_1^{trel}$ is merging to.

(c). If there is no possible value for $\varphi_2^{trel}$, go back to (b) and choose another possible value for $\varphi_1^{trel}$. Then, a new subset of all possible values for $\varphi_2^{trel}$ from $\psi_2^{trel}$ can be found. Or, choose one of the possible values for $\varphi_2^{trel}$ and go to the next step where $i = N_T - 2$. Then, the summation terms in (4.22) can be increased again, and we will choose all possible values for $\varphi_3^{trel}$ from $\psi_3^{trel}$, where $\psi_3^{trel}$ is determined by the state that $\varphi_2^{trel}$ is merging to.

(d). Keep the same process until LSD reaches $\varphi_{N_T}^{trel}$. Then, a complete hypothesized transmitted signal vector $\boldsymbol{\varphi}^{trel} = \left[\varphi_1^{trel} \cdots \varphi_{N_T}^{trel}\right]^T$, the output symbols corresponding to a legal path from the $i_{SMI}^{th}$ state, is added into the candidate path list. If there is no other possible value for $\varphi_{N_T-1}^{trel}$, go back and try another possible value for $\varphi_{N_T-2}^{trel}$. In this case, a new subset of all possible values for $\varphi_{N_T-1}^{trel}$ from $\psi_{N_T-1}^{trel}$ can be found. Or, choose another possible value for $\varphi_{N_T-1}^{trel}$ and modify the summation terms in (4.22) again. Then, a new subset of all possible values for $\varphi_{N_T}^{trel}$ from $\psi_{N_T}^{trel}$ can be found. The same process will be repeated until all candidate hypotheses inside the sphere are added into the candidate path list.

The LSD method has to be applied once for a starting state in $I_{SMI}$. To completely evaluate $\Lambda_{i_{SMI}}^{\Omega}\left(\mathbf{s}^j\right)$, we have to apply the LSD algorithm for $C_{SMI}$ times. So, equation(4.11) can be operated at the $j^{th}$ stage.

Use the example in 4.2.1 as an example and show the application of the LSD

algorithm in the BM calculation. When the decoding process is running to the $j^{th}$ stage, assume that the first and third state have the greatest two state metrics. Then, we only need to evaluate $\Lambda_{1,i}\left(\mathbf{s}^j\right)$ and $\Lambda_{3,i}\left(\mathbf{s}^j\right)$, where $i \in \{1,2,3,4\}$. To evaluate $\Lambda_{1,i}\left(\mathbf{s}^j\right)$, the LSD is initiated from the first state in the trellis diagram. According to the procedure (a), we start from $i=4$ and do not consider the rest terms, $i=1\cdots 3$, in the summation in (4.22). Then, (4.22) is degenerated to

$$\begin{aligned} & u_{4,4}^2 \cdot \left|\varphi_1^{trel} - y_1\right|^2 \le {r_{LSD}}^2 \\ \Rightarrow & \left|\varphi_1^{trel} - y_1\right| \le \frac{r_{LSD}}{u_{4,4}} \end{aligned} \tag{4.25}$$

We choose all possible values for $\varphi_1^{trel}$ satisfying (4.25) from $\psi_1^{trel} = \{0,14,3,13\}$, where $\psi_1^{trel}$ is composed of all branches starting from the first state. Note that the numbers in the subset $\{0,14,3,13\}$ are the decimal number transformed from the constellation points in 16-QAM. If $\varphi_1^{trel} = "14"$ is assumed at (a), $\psi_2^{trel} = \{12,2,15,1\}$ will be obtained at (b). Following the decoding process in (a), (b), (c) and (d), we can find all candidate hypotheses inside the sphere. To evaluate $\Lambda_{3,i}\left(\mathbf{s}^j\right)$, we initiate another LSD detector from the third state. The process is similar to what described above except now $\psi_1^{trel} = \{11,5,8,6\}$. Then, we can have $\Lambda_{1,i}\left(\mathbf{s}^j\right)$ and $\Lambda_{3,i}\left(\mathbf{s}^j\right)$ for its corresponding $i^{th}$ state. Finally, ACS will be applied at each of the four ending states. The block diagram of the MIMO-OFDM receiver for TICM using the LSD detector is shown in Fig. 4-8.

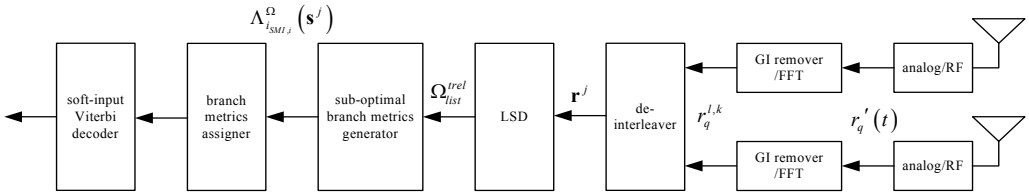


Fig. 4-8: The block diagram of the MIMO-OFDM receiver using SMI and LSD for TICM

### 4.2.3 Choosing the Radius of Sphere for LSD

The size of the candidate path list determines how well (4.11) can approach (4.9). If the radius is too small, the symbol vectors in $\Omega^{trel}_{list}$ may not include the output symbols corresponding to the ML path. If the radius is too large, the LSD detector will find too many candidate paths and the required computational complexity is high. Consider the output symbol sequences corresponding to the ML path $\boldsymbol{\varphi}^{ML-path}$. We have

$$\left|\mathbf{r}-\mathbf{H}\cdot\boldsymbol{\varphi}^{ML-path}\right|^2=\left|\mathbf{n}\right|^2\sim\sigma^2\cdot\chi^2_{N_T} \tag{4.26}$$

where $\chi^2_{N_T}$ is a random variable obeying chi-square distribution with $N_T$ degrees of freedom. The expected value of the sum of the squared noise is $\sigma^2\cdot E\left\{\chi^2_{N_T}\right\}=\sigma^2\cdot N_T$. So, we may choose the radius of the sphere as

$$\begin{aligned} r_{LSD}{}^2 &= \sigma^2\cdot C_{LSD}\cdot N_T-\mathbf{r}^H\cdot\left(\mathbf{I}-\bar{\mathbf{H}}\cdot\left(\bar{\mathbf{H}}^H\cdot\bar{\mathbf{H}}\right)^{-1}\cdot\bar{\mathbf{H}}^H\right)\cdot\mathbf{r} \\ &\approx \sigma^2\cdot C_{LSD}\cdot N_T \end{aligned} \tag{4.27}$$

where $C_{LSD}$ represents a real-valued constant greater than 1. When a suitable value for $C_{LSD}$ is given, the radius of the sphere can be determined. Occasionally, there may be some states having no incoming branches within $\Omega^{trel}_{list}$, the BMs of these states can be replaced by a real-valued constant greater than $r_{LSD}{}^2$.

## 4.3 Simulation Results

In this section, simulations are conducted to evaluate the performance of the

proposed coding scheme. Three different systems with the same throughput are considered. An optional mode is considered, in which the constraint length of CC encoder is 7, the channelization bandwidth is 20MHz (56 occupied sub-channels), and the transmitted spatial streams is 4 ( $N_T = 4$ ).The number of receive antennas is the same as that of transmit antennas.

(a). MIMO-OFDM system with BICM: The simulation platform is based on the TGn Sync proposal. An MMSE equalizer and a simplified soft-bit demapper are used at the receiver. Also, a soft-input Viterbi decoder with trace back length of 128 is used to detect the information bits. We call the system as BICM-EQL.

(b). MIMO-OFDM system with BICM: The simulation platform is based on the TGn Sync proposal. A LSD detector and a vector demapper are used at the receiver, and a soft-input Viterbi decoder with trace back length of 128 is used to detect the information bits. We call the system as BICM-LSD

(c). MIMO-OFDM system with TICM: The simulation platform is based on what we introduced in Chapter 4. A modified soft-input Viterbi decoder with trace back length of 128 is used to detect the information bits. Suboptimal algorithms outlined in this chapter are used. We call the system as TICM-LSD.

Assume that frequency offset and timing offset are perfectly compensated at the receiver. The MIMO channel is perfectly known at the receiver. The PPDU length is set as 1000 bytes; so there are 8000 information bits per package. The preamble format for TICM is assumed to be the same with for BICM. The standard per-tone channel estimation method (no smoothing) is used to estimate the MIMO channel. Simulation results are shown in Fig. 4-9 to Fig. 4-16. For all cases, BICM-EQL performs far worse than BICM-LSD and TICM-LSD. From Fig. 4-9 and Fig. 4-11, we observe that TICM-LSD outperforms BICM-LSD about 1dB improvement in 16-QAM, and 3dB in 64-QAM under channel-B environment respectively. From Fig.

4-10 and Fig. 4-12, we can see that under channel-D environment, BICM-LSD and TICM-LSD have similar performance. However, BICM-LSD performs better in higher SNR regions, while TICM-LSD performs better in lower SNR regions. For SNR around 15.5 dB (for 16-QAM) or 23 dB (for 64-QAM), both methods have similar performance.

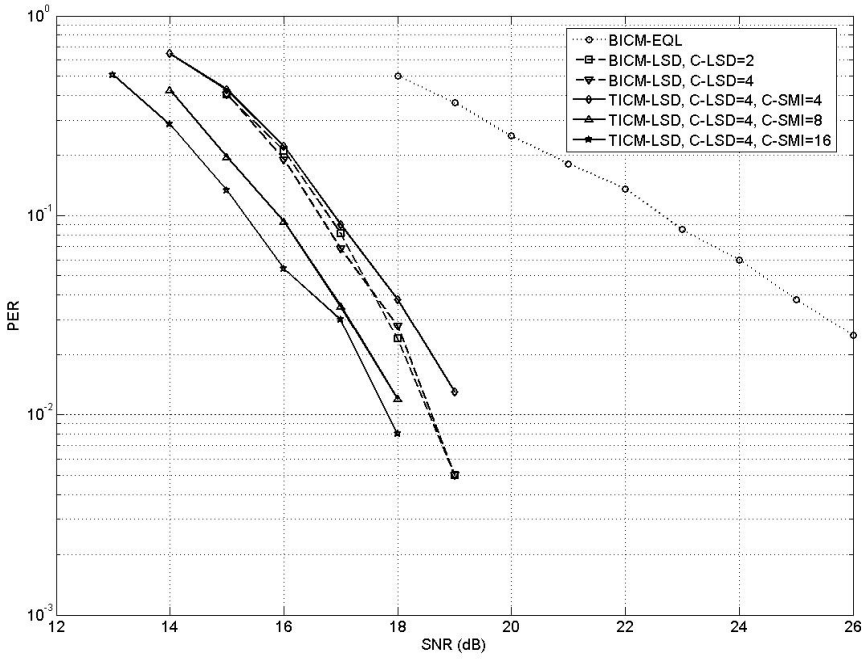


Fig. 4-9: Performance comparison of BICM-EQL, BICM-LSD, and TICM-LSD (20MHz, 4x4, 16-QAM, channel-B, perfect-channel)

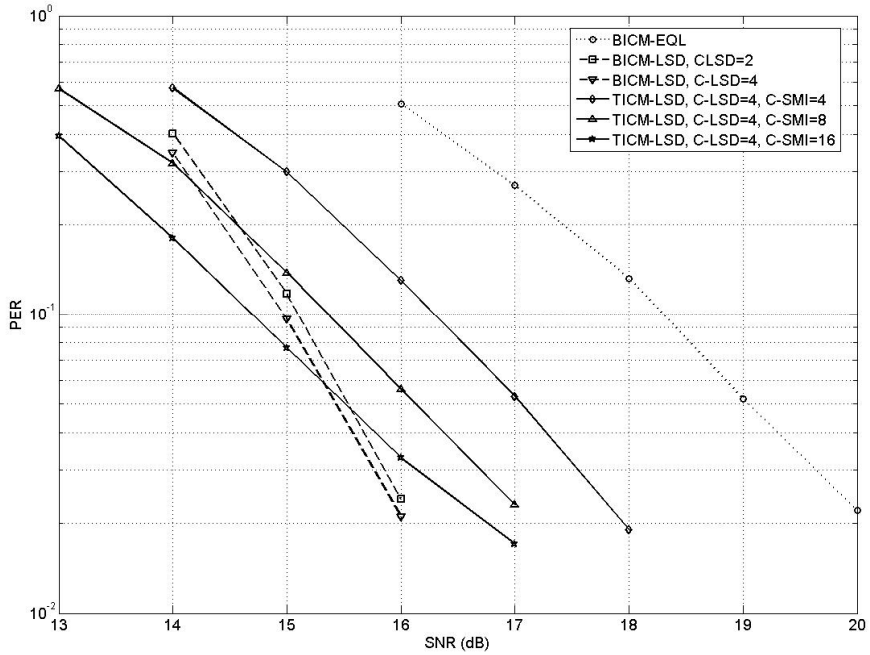


Fig. 4-10: Performance comparison of BICM-EQL, BICM-LSD, and TICM-LSD (20MHz, 4x4, 16-QAM, channel-D, perfect-channel)

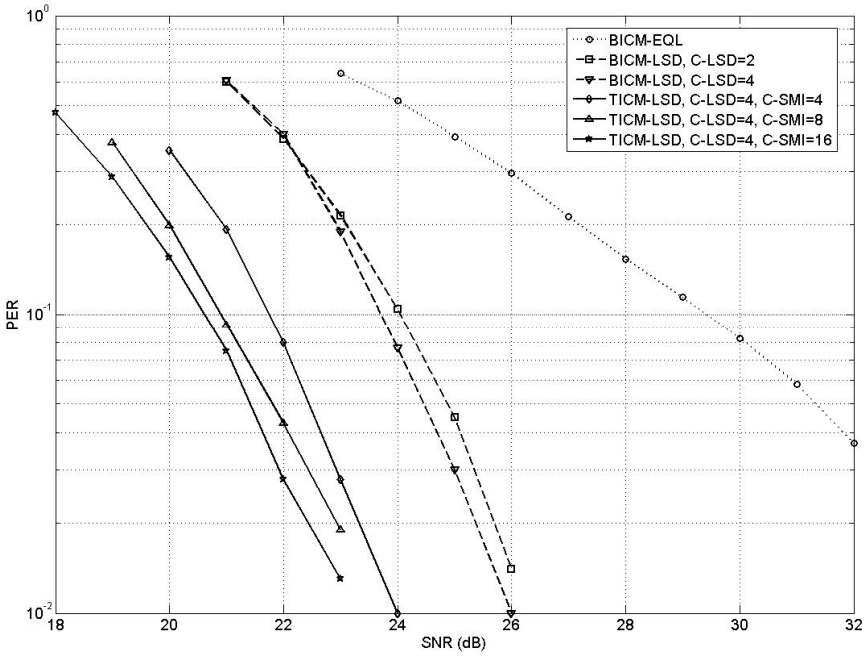


Fig. 4-11: Performance comparison of BICM-EQL, BICM-LSD, and TICM-LSD (20MHz, 4x4, 64-QAM, channel-B, perfect-channel)

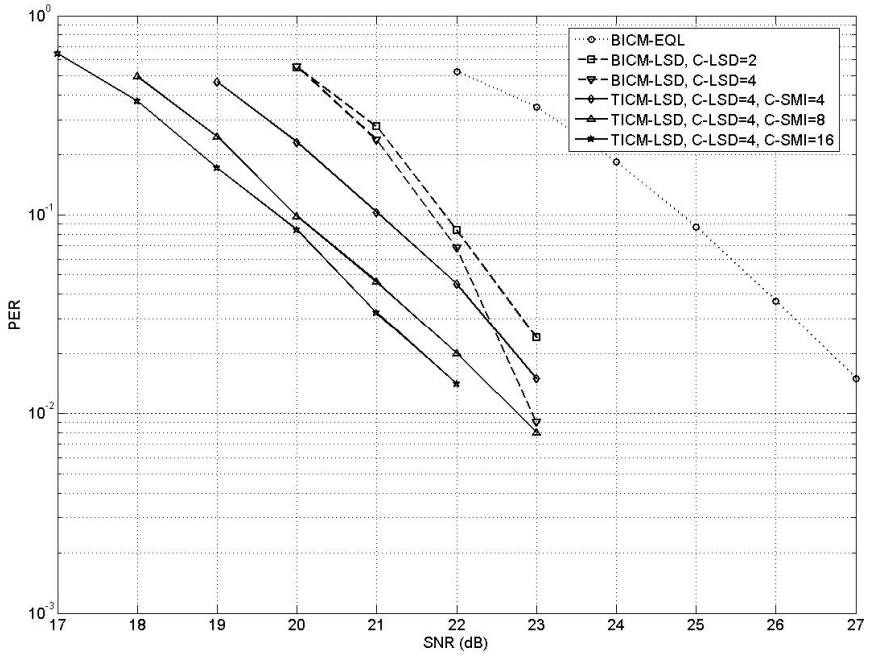


Fig. 4-12: Performance comparison of BICM-EQL, BICM-LSD, and TICM-LSD (20MHz, 4x4, 64-QAM, channel-D, perfect-channel)

It is assumed that perfect channel is known at the receiver in above simulations. In what follows, we will consider the cases with estimated channel. From Fig. 4-13 and Fig. 4-15, we see that TICM-LSD still outperforms BICM-LSD about 1dB in 16-QAM, and 3dB in 64-QAM under channel-B environment respectively. From Fig. 4-14 and Fig. 4-16, we also see the behavior is similar to what observed in cases with perfect channel.

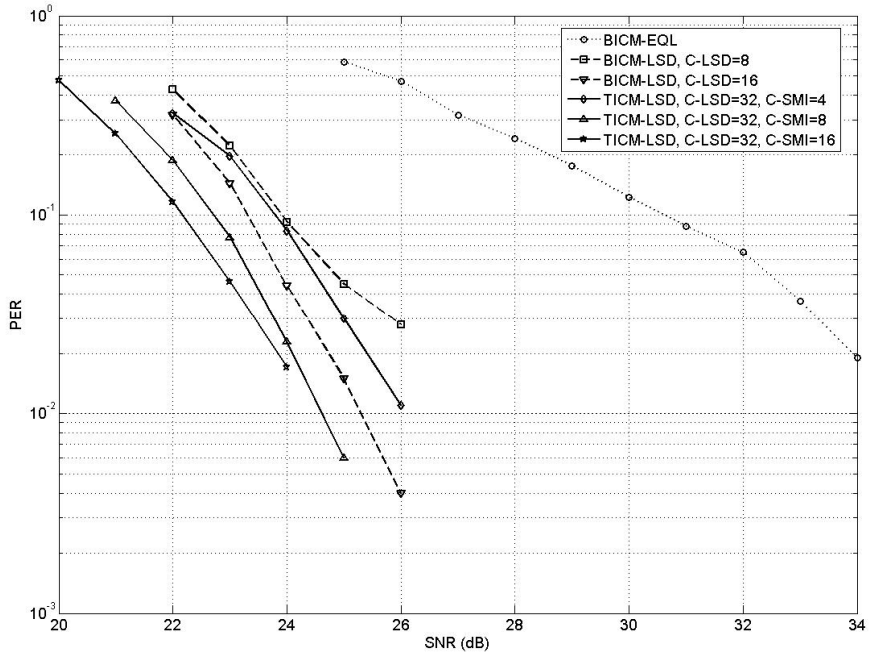


Fig. 4-13: Performance comparison of BICM-EQL, BICM-LSD, and TICM-LSD (20MHz, 4x4, 16-QAM, channel-B, estimated-channel)

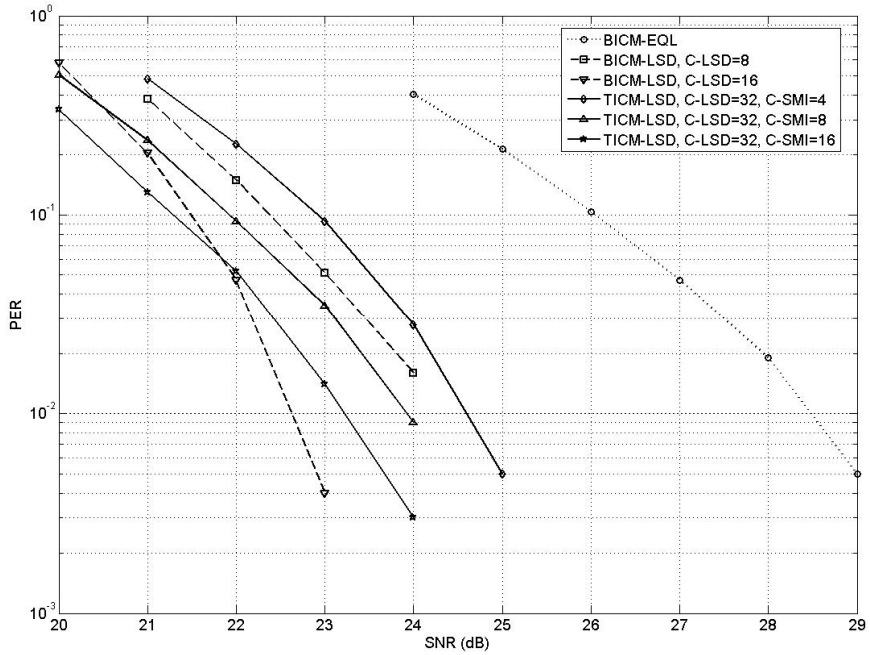


Fig. 4-14: Performance comparison of BICM-EQL, BICM-LSD, and TICM-LSD (20MHz, 4x4, 16-QAM, channel-D, estimated-channel)

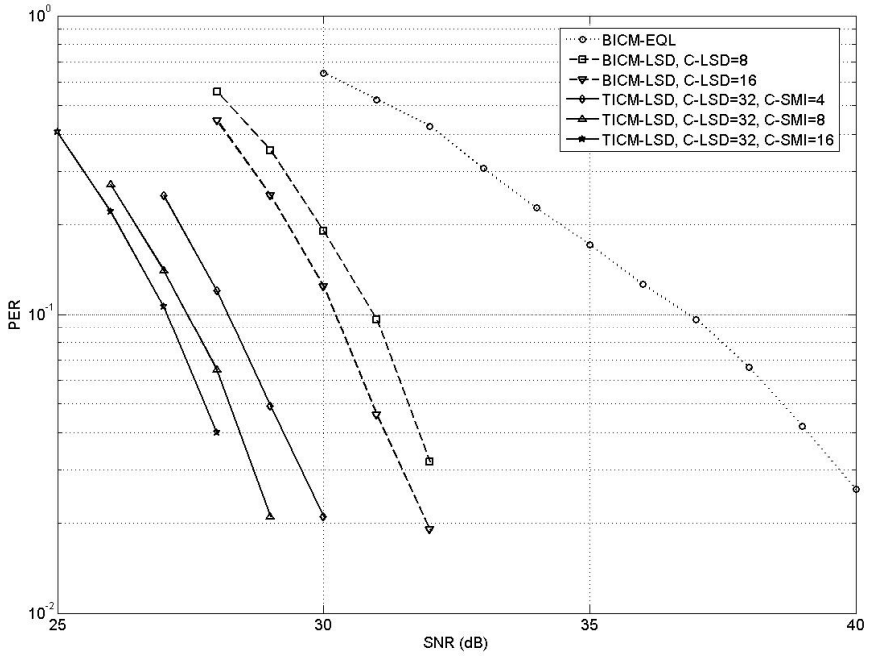


Fig. 4-15: Performance comparison of BICM-EQL, BICM-LSD, and TICM-LSD (20MHz, 4x4, 64-QAM, channel-B, estimated-channel)

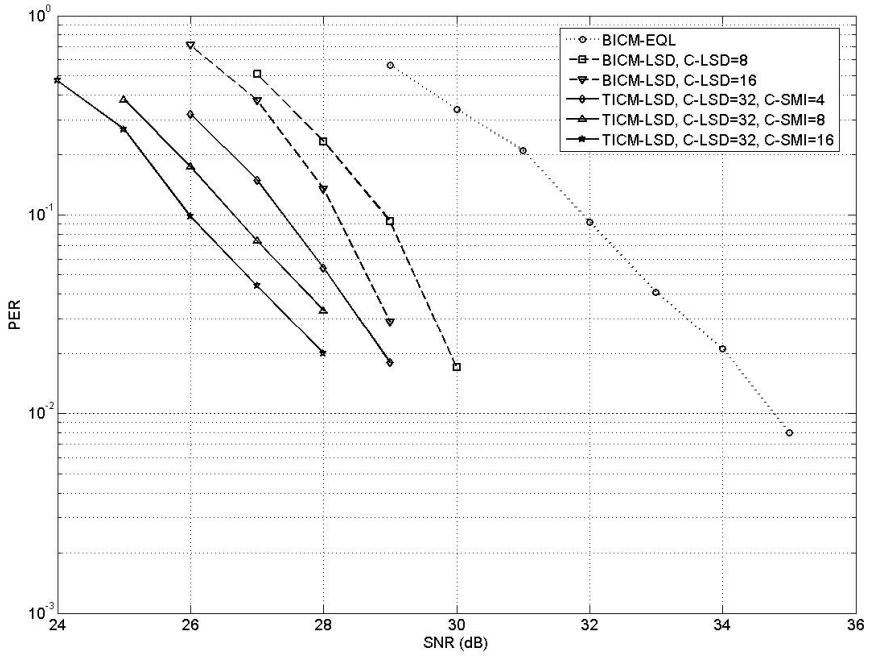


Fig. 4-16: Performance comparison of BICM-EQL, BICM-LSD, and TICM-LSD (20MHz, 4x4, 64-QAM, channel-D, estimated-channel)

Since channel-D has longer multi-path delay spread than channel-B, it is more frequency-selective then channel-B. So, the bit-level interleaver in BICM under channel-D performs better than that in channel-B. In high SNR, the fading channel effect dominates the performance instead of the noise. This explains why BICM-LSD performs better in high SNR region than TICM-LSD under channel-D environment.

## 4.4 Complexity Analysis

In this subsection, we analyze the computational complexity of the systems compared above. We count the number of required multiplications (for the LSD detector) performed by BICM with complex-valued LSD, BICM with real-valued LSD, TICM with complex-valued LSD for $C_{SMI}=4$, and TICM with complex-valued LSD for $C_{SMI}=8$ at each stage. Table 4-1 compares the average number of required multiplications (under channel-B) for four systems.

| | BICM with complex-valued LSD for $C_{LSD}=16$ | BICM with real-valued LSD for $C_{LSD}=16$ | TICM with complex-valued LSD for $C_{LSD}=32$ and $C_{SMI}=4$ | TICM with complex-valued LSD for $C_{LSD}=32$ and $C_{SMI}=8$ |
|---|---|---|---|---|
| SNR=27 (dB) | 1.80E+05 | 4.71E+04 | 2.44E+03 | 4.79E+03 |
| SNR=30 (dB) | 5.45E+04 | 1.08E+04 | 1.19E+03 | 2.30E+03 |
| SNR=33 (dB) | 1.67E+04 | 3.08E+03 | 675.854 | 1.28E+03 |

Table 4-1: The average number of required multipliers for LSD detector (20MHz, 4x4, 64-QAM, channel-B, estimated-channel)

Table 4-2 shows the similar results under channel-D.

| | BICM with complex-valued LSD for $C_{LSD}=16$ | BICM with real-valued LSD for $C_{LSD}=16$ | TICM with complex-valued LSD for $C_{LSD}=32$ and $C_{SMI}=4$ | TICM with complex-valued LSD for $C_{LSD}=32$ and $C_{SMI}=8$ |
|---|---|---|---|---|
| SNR=27 (dB) | 1.12E+05 | 3.18E+04 | 2.26E+03 | 4.44E+03 |
| SNR=30 (dB) | 2.82E+04 | 6.21E+03 | 1.04E+03 | 2.00E+03 |
| SNR=33 (dB) | 9.49E+03 | 1.75E+03 | 5.26E+02 | 9.88E+02 |

Table 4-2: The average number of required multipliers for LSD detector (20MHz, 4x4, 64QAM, channel-D, estimated-channel)

From Table 4-1 and Table 4-2, we can see that the average number of multiplications for BICM with real-valued LSD is lesser than that with complex-valued LSD. Note that the sphere of the LSD detector in TICM needs to be larger than that in BICM. So, let $C_{LSD}$ for TICM be twice of $C_{LSD}$ for BICM. From Table 4-1, we can see that the average number of multiplication for TICM with $C_{SMI}=8$ ranges from 0.25 and 0.1 of that for BICM with real-values LSD (for PER=0.1 to PER=0.001 under channel-B). From Table 4-2, we can also observe that the average number of multiplications for TICM with $C_{SMI}=8$ range from 0.5 to 0.15 of that for BICM with real-valued LSD (for PER=0.1 to PER=0.001 under channel-D).

# Chapter 5 Conclusions and Future Works

## 5.1 Conclusions

The BICM scheme is a well know scheme for coded systems. For MIMO systems, the receiver usually uses an equalizer and a soft-bit demapper to obtain soft-bit information. Combining with the Viterbi algorithm, it provides a simple and straightforward decoding scheme. However, this approach is not optimal and its performance will be greatly degraded in typical MIMO channel environments. Although the optimum soft-bit demapping can be applied, its computational complexity is high. In this thesis, we study the outer receiver design of IEEE 802.11n system and also propose a new modulation-coding scheme called TICM for MIMO-OFDM systems. Simulations show that BICM with LSD can provide significant improvement over that with the MMSE equalizer and multiple soft-bit demappers. Also, the proposed TICM can have lower computational complexity and is more suited to channels with short responses. With multiple transmit antennas and large QAM size, TICM can significantly reduce the computational complexity and the required memory size. The more antennas the transmitter has and the larger the QAM size is, the more efficient the TICM can be.

## 5.2 Future Works

In concluding the thesis, we outline the potential topics for further research. First, we may jointly optimize the CC encoder and the QAM mapper at the transmitter, since the gray-like mapping may not be optimal for TICM. Second, the LSD detector used in TICM can be modified into a real-valued one with extra control units. This can reduce the computational complexity furthermore. Finally, an outer code may be concatenated with the CC encoder in TICM to enhance the performance. With turbo

principle, a new interleaver added between the inner and outer codes can compensate the weakness of the original tone-level interleaver.

# Reference


[1]. C. Berru, A. Glavieux and P.Thitimajshima, “Near Shannon limit error-correcting coding and decoding: turbo codes,” *Int. Conf. Commun.*, pp. 1064-1070, 1993.

[2]. R. G. Gallager, *Low Density Parity Check Codes*, MIT Press, Cambridge, Massachusets, 1963.

[3]. C. E. Shannon, “A mathematical theory of communication,” *Bell Syst. Tech. J.*, vol. 27, pp. 379-423 (Part one), pp. 623-656 (Part two), Oct. 1948.

[4]. E. Telatar, “Capacity of multi-antenna Gaussian channels,” *European Trans. on Telecommunications*, vol. 10, no. 6, pp. 585-595, Nov./Dec. 1999.

[5]. G.J. Foschini and M.J. Gans, “On limits of wireless communications in a fading environment when using multiple antennas,” *Wireless Personal Communications*, vol. 6, pp. 311-335, 1998.

[6]. B. R. Salzberg, “Performance of an efficient parallel data transmission system,” *IEEE Trans. on Commun.*, vol. COM-15, pp. 805-811, Dec. 1967.

[7]. S. Weinstein and P. Ebert, “Data transmission by frequency-division multiplexing using the discrete Fourier transform,” *IEEE Trans. on Commun.*, vol. 19, Issue. 5, pp. 628-634, Oct. 1971.

[8]. E. Zehavi. “8-PSK trellis codes for a rayleigh channel,” *IEEE Trans. on Commun.*, vol. 40, pp.873-884, May 1992.

[9]. F. Tosato and P. Bisaglia, “Simplified soft-output demapper for binary interleaved COFDM with application to HIPERLAN/2,” *IEEE Int. Conf. on Commun.*, vol. 2, pp. 664-668, 2002.

[10]. U. Fincke and M. Pohst, “Improved methods for calculating vectors of short length in a lattice, including a complexity analysis,” *Math. Computation*, vol. 44, pp. 463-471, Apr. 1985.

[11]. Bertrand M. Hochwald and Stephan ten Brink, “Achieving near-capacity on a multiple-antenna channel,” *IEEE Trans. on Commun.*, vol. 51, no. 3, pp. 389-399, Mar. 2003.

[12]. A. J. Viterbi, “Error bounds for convolutional codes and an asymptotically optimum decoding algorithm,” *IEEE Trans. Inform. Theory*, IT-13, pp. 260-269, 1967.

[13]. IEEE 802.11a-1999, *Part 11: Wireless LAN Medium Access Control (MAC) and Physical Layer (PHY) specifications: High-speed Physical Layer in the 5 GHz Band*, Sept. 1999.

[14]. S. A. Mujtaba, IEEE 802.11 document 04/889/r7 “TGn Sync proposal technique specification,” July 2005.

[15]. V. Erceg et al., IEEE 802.11 document 03/940r4 “TGn channel models,” May 2004.

[16]. S. A. Mujtaba, IEEE 802.11 document 04/891/r7 “TGn Sync proposal phy results,” July 2005.

[17]. A. P. Stephens, IEEE 802.11 document 03/814/r31 “”TGn comparison criteria,” July 2004.

[18]. J. Benesty, Y. A. Huang and J. Chen, “A fast recursive algorithm for optimum sequential signal detection in a BLAST system,” *IEEE Trans. on Signal Processing*, vol. 51, no. 7, pp. 1722-1730, July 2003.

[19]. S. H. Muller-Weinfurtner, “Coding approaches for multiple antenna transmission in fast fading and OFDM,” *IEEE Trans. on Signal Processing*, vol. 50, no. 10, pp. 2442-2450, Oct. 2002.

[20]. S. A. Mujtaba, IEEE 802.11 document 04/890/r3 “TGn Sync proposal FRCC compliance,” Mar. 2005.